Geophysical Journal International

Geophys. J. Int. (2022) **230,** 298–316
Advance Access publication 2022 February 23
GJI Seismology

https://doi.org/10.1093/gji/ggac079

The Moho reflectivity of the subduction beneath the Southwestern Alps from ambient seismic noise autocorrelations

T.N. Ashruf[1,2] and A. Morelli[1,2]

[1]*Dipartimento di Fisica e Astronomia, Alma Mater Studiorum - Università di Bologna, Via Zamboni* 33, 40126 *Bologna, Italy. E-mail: tahira.ashruf@ingv.it*
[2]*Istituto Nazionale di Geofisica e Vulcanologia, Sezione di Bologna, Via Donato Creti* 12, 40128 *Bologna, Italy*

Accepted 2022 February 21. Received 2022 February 18; in original form 2021 April 14

SUMMARY

The Western Alps shows a complex crustal organization due to the subduction of the European Plate beneath the Adriatic Plate and exhumation of the mantle wedge. The lithospheric structure of the Western Alps, that may hold significance for understanding orogenic processes and evolution, has been the subject of many geophysical studies, but the Moho profile remains unclear and this has led to controversies about the depth and extent of the European Plate beneath the Adriatic Plate. With the goal of retrieving detailed information on crustal constitution, we use autocorrelation of seismic ambient noise as a tool to map the body wave reflectivity structure at the subduction zone under the southwestern Alps. We use data recorded by the China–Italy–France Alps (CIFALPS) seismic transect, that includes 45 stations located approximately 5–10 km apart along a profile crossing the Alpine continental subduction in the Western Alps. We analyse the data set in four different frequency bands between 0.09 and 2 Hz. We automatically pick the arrival time of the Moho reflection in the second derivative of the envelope of the autocorrelation stack using prior Moho information. The 0.5–1 Hz frequency band mostly gives the best result due to the clear changes in reflectivity along the waveforms of the autocorrelation stacks after the picked arrival times of the Moho reflections. We find spatial coherence between 18 and 23 km depth in the western portion of the profile, indicating relatively homogeneous crustal rocks, and highly reflective structure under the central mountain range, due to the existence of a highly faulted zone. The very thin crust and the underlying mantle wedge known as the Ivrea body show instead high transparency to seismic waves and absence of reflections. The subduction profile of the European Plate shows a steep trend as compared to previous studies. We discuss autocorrelation stacks and Moho depths obtained from the arrival times of the picked reflectivity change in comparison with previous studies to validate the different reflection structures. Stacked ambient noise autocorrelations reliably image varied crustal properties and reflectivity structures in the highly heterogeneous region of the southwestern Alps.

Key words: Europe; Body waves; Seismic interferometry; Seismic noise; Crustal structure.

1 INTRODUCTION

The complex geological structure involved in the Alpine orogeny is the result of the European and Adriatic plates converging motion in a process marked by subduction, accretion and transformation (e.g. Handy *et al.* 2010; van Hinsbergen *et al.* 2020). This region has been the subject of many geological and geophysical studies focused on understanding its geodynamic evolution, leading to controversial results regarding, for example the amount of crustal subduction under the Alps (e.g. Grellet *et al.* 1993; Thouvenot *et al.* 2007). In fact, the subduction of the European plate underneath the Adriatic Plate during the Cretaceous to Palaeogene (e.g. Handy *et al.* 2010) has led to complex variation in Moho depths along the Western Alps, especially in the southwestern Alps. This specific area has been probed by several seismological studies. The controlled source seismological study by Grellet *et al.* (1993) mapped the Moho depth between 47 and 50 km, whereas using the same approach Thouvenot *et al.* (2007) measured a deeper Moho, down to 55 km, providing evidence of the crustal root being much thicker. Nicole *et al.* (2007) and Diehl *et al.* (2009) have used local earthquake data to image the 3-D velocity structure. The latter study was able to gather detailed information of the Ivrea body and the European crust underneath the Adriatic crust down to a depth of 45 km. In addition, the southwestern Alps have been the subject of various studies

using teleseismic earthquake records (e.g. Lombardi *et al.* 2008; Zhao *et al.* 2015; Beller *et al.* 2018). In the receiver function study by Lombardi *et al.* (2008) the Moho reached depths of about 55 km beneath some stations, however only sparse information was available for the southwestern Alps due to the few stations in the area. In 2012 the China–Italy–France Alps seismic survey (CIFALPS) deployed a passive seismic profile cutting completely through the southwestern Alps (see Map in Fig. 1) to improve the constraints on the lithospheric structure, with emphasis on the Moho geometry. Zhao *et al.* (2015) used the teleseismic earthquake records of the CIFALPS data set to create *P* receiver functions and claimed the first seismic evidence of continental subduction down to 75 km depth beneath the southwestern Alps. Beller *et al.* (2018) used the same data set and applied a teleseismic full-waveform inversion method that resulted in Moho depths down to 80–90 km for the v_S model. Furthermore, Lu *et al.* (2018) and Kästle *et al.* (2018) have created shear wave velocity models by extracting surface wave information from cross-correlation of ambient seismic noise. Lu *et al.* (2018) imaged shallower Moho depths than Zhao *et al.* (2015) beneath the Southeast Basin that is situated at the western end of the CIFALPS profile (Fig. 1). In addition, Lu *et al.* (2018) obtained *a posteriori* probability densities of interfaces by Bayesian inversion that resulted in a very low probability for the Moho discontinuity at 45–90 km depth beneath the Ivrea body. The results by Kästle *et al.* (2018) imaged also shallower Moho depths beneath the Southeast Basin and reached a maximum depth of 60 km for continental subduction as opposed to the deeper subductions by previous teleseismic studies. The results of these studies give clear evidence of the uncertainties on the crust–mantle transition zone in the southwestern region of the Alpine belt.

Seismic interferometry is a method to obtain the Green's function between two seismic receivers by cross-correlating the recorded seismic wavefield. The impulse response or Green's function is thus obtained at one receiver as produced by a virtual source at the position of the other receiver (e.g. Roux *et al.* 2005). In recent years, passive seismic interferometry has become a standard tool that uses ambient seismic noise for investigating the Earth structure between two receivers (e.g. Nakata *et al.* 2019) by obtaining surface wave dispersion. However, imaging sharp discontinuities such as the Moho are difficult because the surface wave velocities reconstructed from ambient noise cross-correlations are not explicitly sensitive to the depth of layer boundaries. When the distance between the two receivers decreases to zero, the cross-correlation becomes the autocorrelation of signal recorded at a single station. The autocorrelation is a zero-offset reflection response by assuming a collocated source and receiver. Claerbout (1968) has shown that the autocorrelation for a vertically incident plane acoustic wave transmitted through a layered structure with a free surface provides sufficient information to recover the reflection response of the medium, including free surface multiples. This can also be applied to ambient noise. In this case, the surface wave component loses its dominance and the body wave interaction with the structure beneath the station increases in importance. Wapenaar *et al.* (2008) have shown that seismic interferometry works for suitable noise conditions without any earthquake or man-made sources. Therefore, ambient noise seismic data becomes a powerful tool to study sharp discontinuities.

In the last decade, autocorrelation of ambient seismic noise has often been used to image the Earth structure beneath seismic stations. Tibuleac & von Seggern (2012) created noise autocorrelations on three components of seismic stations in Nevada to extract Moho-reflected body wave phases in the 0.5–1.0 Hz frequency band. Oren & Nowack (2016) found similar results as Tibuleac & von Seggern (2012) by creating noise autocorrelations using different processing techniques in Nevada and the central U.S.A. using different cut-off frequencies between the 0.2 and 0.75 Hz range. Gorbatov *et al.* (2013) computed noise autocorrelations in the 2.0–4.0 Hz range on the vertical component of stations in Australia to create Moho depth maps. Similar studies have been performed in Australia by Kennett *et al.* (2015) in the 2.0–4.0 frequency band, and by Kennett (2015) with different cut-off frequencies in the 0.5–4.0 Hz range. Taylor *et al.* (2016) imaged the crustal structure of the North Anatolian Fault zone in Turkey by bandpass filtering the autocorrelations in the 0.2–0.4 Hz frequency band. Saygin *et al.* (2017) mapped the *P*-wave reflection response of the Jakarta Basin, Indonesia in the 2.0–4.0 Hz frequency band. The Ebro Basin in Spain was mapped by Romero & Schimmel (2018) using ambient noise autocorrelations, where the data were significantly filtered in broader frequency ranges with the lower and upper corner frequencies ranging between 3.0–4.0 Hz and 9.0–18.0 Hz, respectively. In Central and Eastern Europe, Becker & Knapmeyer-Endrun (2018) and Becker & Knapmeyer-Endrun (2019a) extracted the crustal thickness from noise autocorrelations in the 1.0–2.0 Hz and 2.0–4.0 Hz frequency bands for, respectively, the vertical and horizontal component data. The detection of the Moho reflectivity depends on the character of the discontinuity. The Moho coincides with a prominent body wave reflection when the discontinuity is sharp (Tibuleac & von Seggern 2012; Gorbatov *et al.* 2013; Phạm & Tkalčić 2017). However, when the discontinuity is marked by a gradational transition between the crustal and mantle wave speed, the detection of the Moho becomes less clear and additional independent information is needed (Kennett 2015; Kennett *et al.* 2015; Becker & Knapmeyer-Endrun 2018, 2019a). Kennett (2015) has shown that in areas with a gradational Moho discontinuity, the base of the crustal reflectivity fits well with the Moho. In addition, Becker & Knapmeyer-Endrun (2018) have shown that the base of crustal reflectivity coincides with the local maximum of the second derivative of the envelope of the autocorrelation, thus providing a criterion useful for automatic detection of the interface. From the shear wave velocity models by Lyu *et al.* (2017) it is clear that the Western Alps are characterized by a gradational Moho.

In this study, we estimate zero-offset reflection responses using ambient noise autocorrelations with the aim of imaging the subduction of the European plate underneath the Adriatic micro plate in the southwestern Alps. We use prior Moho information by Zhao *et al.* (2015) to follow the principle proposed by Becker & Knapmeyer-Endrun (2018) for selecting the reflection coinciding to the gradational Moho. After a detailed description of our processing workflow, we present the results of the automatically and manually picked arrival times of Moho reflections for different frequency bands. Further, we discuss the results and geological features detected along the cross-section compared to the geological features from previous studies.

2 DATA AND METHOD

We use the ambient seismic noise data recorded by the broad-band CIFALPS (China–Italy–France Alps) seismic survey (Zhao *et al.* 2016). The 46 seismic stations of the network were set up through the southwestern Alps with an interstation distance of 5–10 km and operated for 14 months between 2012 and 2013 (see station map in Fig. 1). Station CT37 is discarded due to instrumental problems for the majority of the days and it is marked by a red filled star in Fig. 1. The seismic waveform data of the vertical channels (HHZ) were downloaded from the Résif Seismological data portal (Zhao

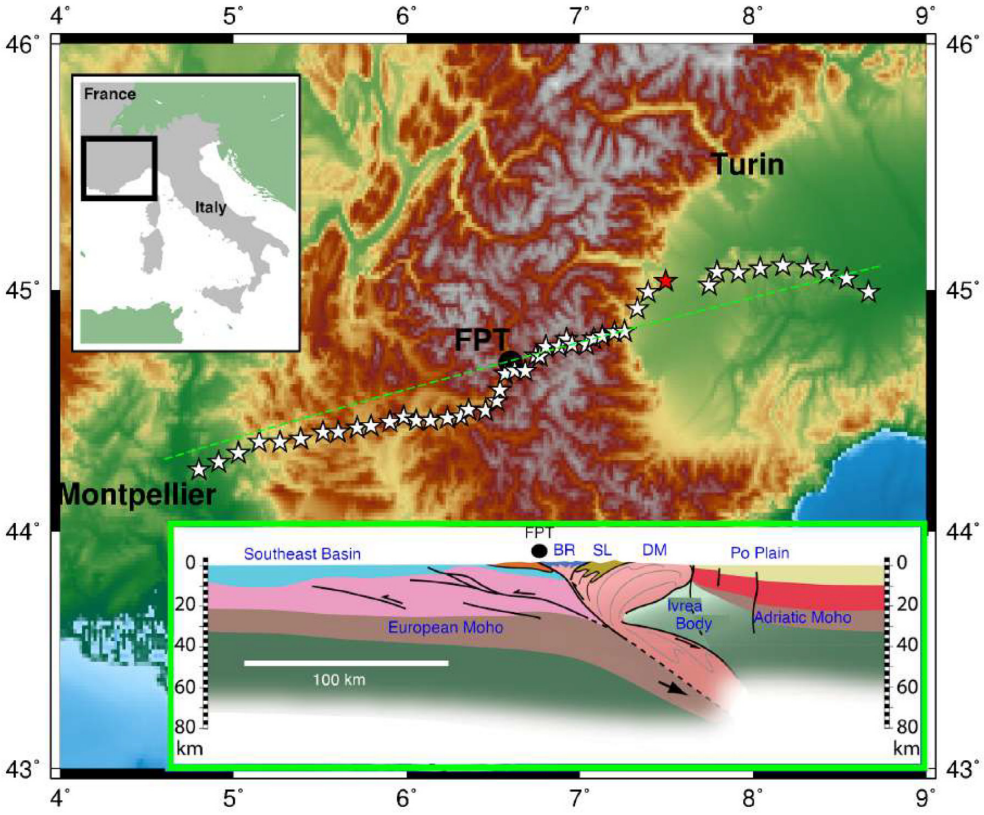

Figure 1. Map of CIFALPS stations, marked by white stars, plotted on topographic elevation. The red star is the discarded station CT37. The black circle marks the Frontal Penninic thrust (FPT) through which the dotted green line goes. This dotted line is the reference profile used for projections to compare the final results to the receiver function study by Zhao *et al.* (2015). The crustal-scale geological interpreted cross section by Zhao *et al.* (2015) along the reference profile is shown in the bottom right-hand figure. BR, Brianconnais; SL, Schistes Lustres; DM, Dora Maira.

et al. 2016) and have a sample rate of 100 Hz. In this work, we only use the vertical components since our focus lies on the reflected *P*-wave energy that is expected to travel with vertical incidence. We use the term reflectivity for the reflected *P*-wave energy travelling at vertical incidence.

In this section, we first describe the range of frequency that has been chosen for imaging body wave reflections from ambient noise autocorrelations. Afterwards, we outline the processing steps for creating autocorrelation stacks for each station. At last, we show the Moho signature that is picked from the second derivative envelope of the autocorrelation stacks. This method is based on the study by Becker & Knapmeyer-Endrun (2018).

2.1 Ambient noise frequency ranges

Although more than 50 yr ago Claerbout (1968) has shown that body waves extracted from autocorrelations provide the reflection response of the medium below the station, only in the last decade this method has been used in passive seismological studies (e.g. Tibuleac & von Seggern 2012; Becker & Knapmeyer-Endrun 2018). However, so far there is no standard procedure and frequency range to be used for extracting body wave reflections from autocorrelations. The study of the seismic ambient noise on the dominant type of waves in different frequency bands by Ruigrok *et al.* (2011) has shown that the vertical components are dominated by body waves with respect to surface waves in the 0.09–1 Hz frequency band. In addition, Asten (1976) has recorded the dominance of *P* waves microseism energy up to 2 Hz. Seismic ambient noise with frequency above 1 Hz is dependent on more nearby cultural sources and may strongly vary in amplitude based on the location of the station.

Fig. 2 shows the probability density function of the power spectral density (PSD) of the vertical channel, HHZ, of station CT14 (the figure is retrieved from: http://dx.doi.org/10.15778/RESIF.YP2012). The red rectangle highlights the period range of ambient noise that we use in this study to create autocorrelations taking into consideration the body wave dominance on the vertical component. The ocean-generated primary and secondary microseism peaks are marked by the white arrows and labelled, respectively, PM and SM.

From further analysis, we leave out frequencies above 2 Hz, due to the complicated behaviour of the signal at these periods. In this study, the seismic ambient noise will be filtered between 0.09 and 2 Hz using different cut-off frequencies. The cut-off frequencies are based on including or excluding the primary and secondary microseism peak, 0.095 and 0.25 Hz, respectively.

2.2 Autocorrelation workflow

We process raw data using ObsPy (Krischer *et al.* 2015) and Matlab for respectively the first and second processing stages. In the first processing stage of the ambient seismic noise data, we start with subtracting the mean and trend before tapering the ends with a Hanning window width of 0.01. Afterwards, we decimate the data from $f_s = 100$ Hz to $f_s = 20$ Hz. Decimation has been performed to increase the processing speed, while taking into consideration that the highest cut-off frequency, 2 Hz, is well below the Nyquist frequency of 10 Hz. We finish the first processing stage by removing

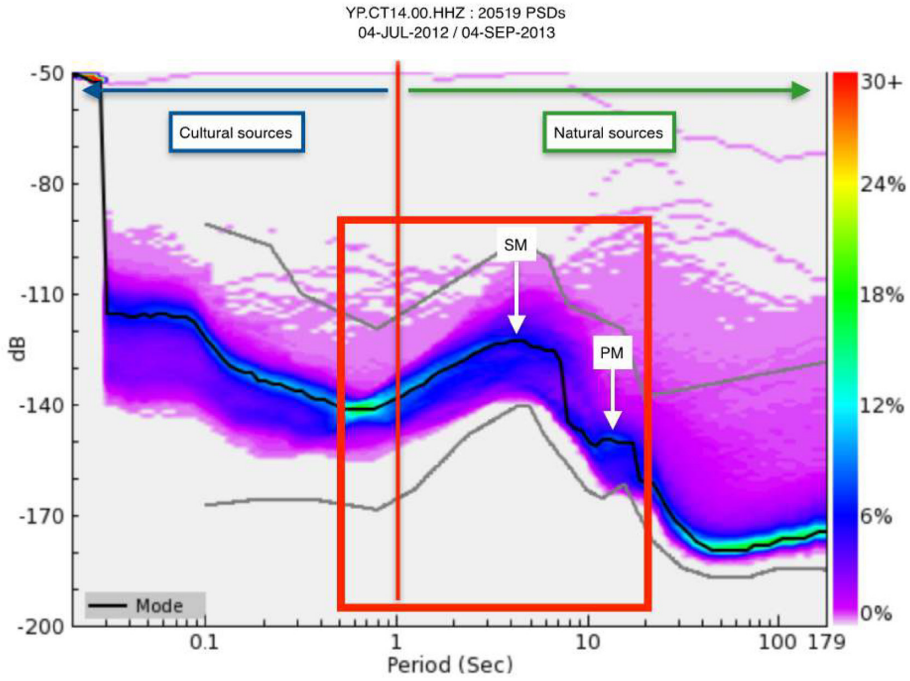

Figure 2. The probability density function of the power spectral densities (PSDs) of station CT14 (figure retrieved from: http://dx.doi.org/10.15778/RESIF.YP2012). The red rectangle marks the period range used in this study, that is dominated by body waves and include the primary (PM) and secondary (SM) microseism peak, 10.5 and 4 s, respectively.

the instrument response over the following trapezoidal frequency range of $f_1 = 0.01$ Hz, $f_2 = 0.02$ Hz, $f_3 = 5$ Hz, $f_4 = 10$ Hz to obtain displacement (nm).

After such preparation, we further process the data with Matlab. Fig. 3 shows the sequential order of steps of the second processing stage to create autocorrelations for sample station CT05 on sample Julian day 201 of 2012. The second processing stage starts with filtering of the data by using a zero-phase two-pole Butterworth bandpass filter in the following passbands (frequencies in Hertz): [0.09–0.5], [0.1–0.5], [0.1–1], [0.3–1], [0.4–1], [0.5–1], [0.5–2] and [1–2]. Bandpass filtering can be applied either before (e.g. Romero & Schimmel 2018) or after (e.g. Oren & Nowack 2016) computation of the autocorrelations. Mroczek & Tilmann (2021) shows that when applying the bandpass filter after computation of the autocorrelations, more processing is needed to prevent the sidelobes of the zero-lag autocorrelation peak from masking the reflection response of the medium. We have applied the bandpass filter before computation of the autocorrelations. After applying the bandpass filter, we cut the time-series into 1-hr time intervals to autocorrelate, Fig. 3(c). In case of an earthquake, waveforms are dominated by high-amplitude wave packets. Bensen *et al.* (2007) showed that the effect of earthquakes and non-stationary sources close to the stations can effectively be removed by applying a time-domain, or temporal, normalization. Therefore, we also apply such sign-bit normalization that only retains information on zero-crossings in the time domain and obliterates amplitude information, Fig. 3(d). Afterwards, we autocorrelate 1-hr data slices, Fig. 3(e), and then linearly stack them for the complete data set.

2.3 Moho reflectivity from autocorrelation stacks

The Moho discontinuity in autocorrelation stacks will not be a single prominent reflector for areas where the transition of the crust to mantle is gradational (e.g. Gorbatov *et al.* 2013; Kennett *et al.* 2015; Kennett 2015). Kennett *et al.* (2015) and Kennett (2015) have shown that the base of the crustal reflectivity fits well with the Moho in areas where the Moho is gradational. Synthetic autocorrelation seismograms by Gorbatov *et al.* (2013) show that in such cases the transition does not originate a simple pulse, such as commonly seen in lower-frequency receiver function studies. Becker & Knapmeyer-Endrun (2018) have used this principle of picking the Moho depth as the base of the crustal reflector by developing an automated method to pick reflectivity changes. The picked reflectivity changes are chosen as the Moho depth if the pick matches a prominent reflectivity change along the waveform of the autocorrelation. Becker & Knapmeyer-Endrun (2018) automatically pick the reflectivity changes by extracting the local maxima inside an *a priori* time window of the 5-s weighted moving average of the second derivative autocorrelation envelope. Their *a priori* time window is based on the uncertainty of the prior Moho information and the velocity model used. The local maxima coincides with large changes in the slope of the envelope and with changes in reflectivity.

We perform an automated pick of changes in reflectivity inside some *a priori* time window, based on Moho depth information from Zhao *et al.* (2015), of the second derivative envelope of the autocorrelation stack. The Moho depth is converted into two-way traveltime (TWT) by using the *P*-wave speed model of Zhao *et al.* (2015), see Fig. S1 in the supplementary file. Fig. 4 shows the method to pick the arrival times of the Moho reflections by automatically picking reflectivity changes from the second derivative of the envelope, applied to stations CT05 and CT07, respectively, in the [0.3–1] and [0.5–1] Hz frequency band. We have not normalized the second derivative envelope, as opposed to Becker & Knapmeyer-Endrun (2018) since there will be no change in the waveform and the arrival time of the local maxima. The *a priori* time window is shown by the grey filled area, Fig. 4, and has a TWT width of 5 s, where the boundaries are set at 2.5 s TWT before and after the *a priori*

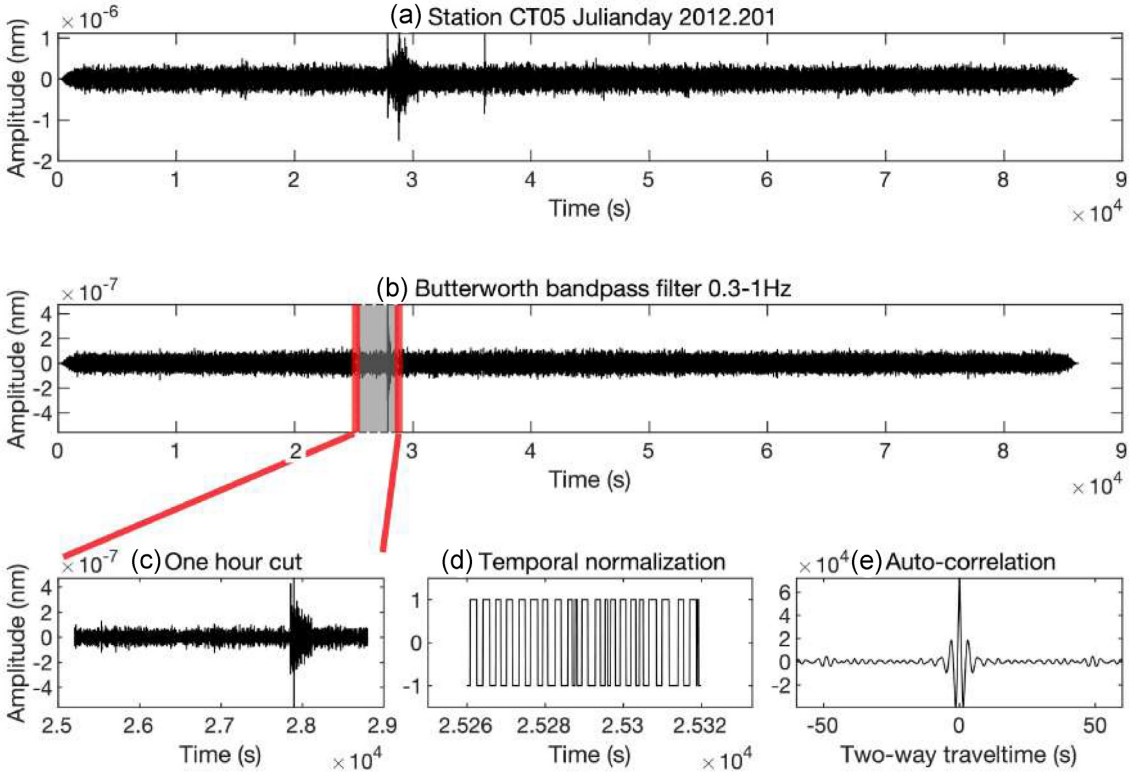

Figure 3. The processing steps performed to create autocorrelations for station CT05 on Julian day 201 of 2012. (a) After removing the mean, trend, tapering the end, decimating and removing the instrument response. (b) Data has been filtered between 0.3 and 1 Hz using a zero-phase Butterworth bandpass filter. (c) 1 hr cut of the day. (d) Temporal normalization and (e) hourly autocorrelation for the complete linear stack.

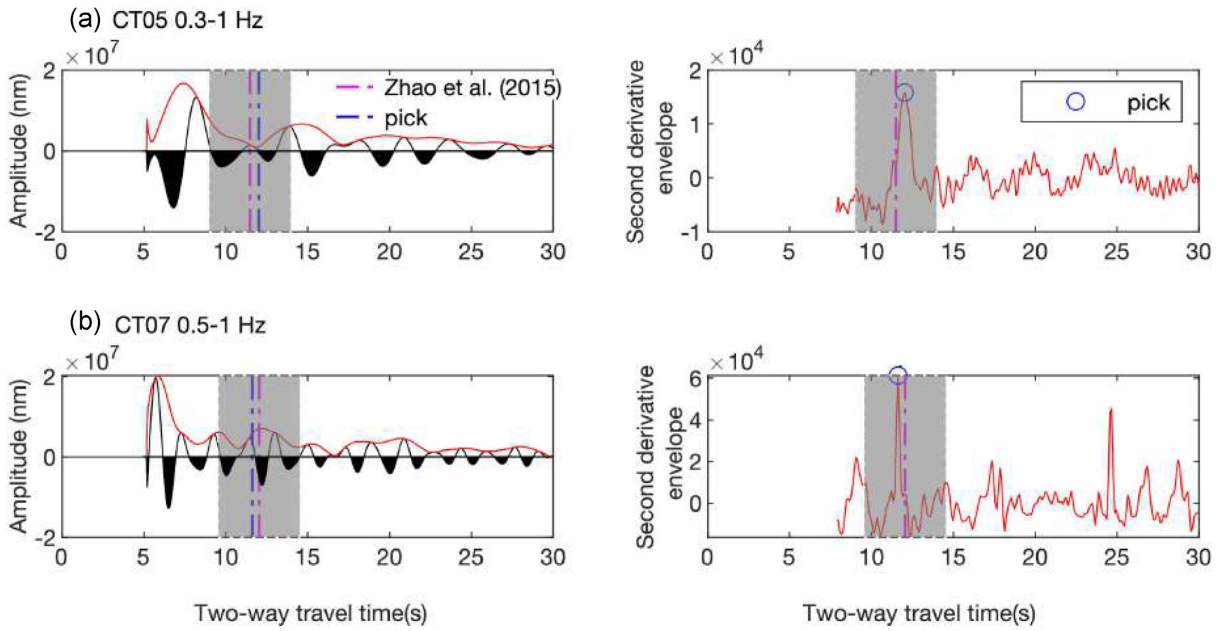

Figure 4. The stacked autocorrelations of station (a) CT05 and (b) CT07 are filtered respectively between the 0.3–1 Hz and 0.5–1 Hz frequency ranges. The stacks are shown on the left with the envelope in red, while the arrival times of the automatically picked reflectivity changes and previous Moho information by Zhao *et al.* (2015) are given by the blue and pink dashed–dotted lines, respectively. The plots on the right-hand side are the second derivative of the envelope, with the local maximum pick inside the *a priori* time window (grey filled area) shown by the blue circle (blue dashed–dotted line in the left-hand plot).

Moho reflection time. The *a priori* time window is not based on the uncertainty of the prior Moho information and velocity model by Zhao *et al.* (2015) since these values are not available. The pink dashed–dotted line corresponds to the prior Moho information and the blue circle and blue dashed–dotted line to the local maximum picked inside the time window. To eliminate the noise of the second derivative of the envelope we use a 5-point moving average filter. We have not weighted the second derivative envelope with a five second

moving average for assigning higher relevance to high amplitude parts (Becker & Knapmeyer-Endrun 2018), since it is equally possible to identify the local maxima related to the reflectivity changes without weighting of the second derivative envelope (Becker & Knapmeyer-Endrun 2019b). Furthermore, the length of the weighting time window has influence on which peaks are favoured because the filtered envelope's amplitude decay is controlled by the bandpass used (Helffrich 2019; Becker & Knapmeyer-Endrun 2019b).

3 RESULTS

We present autocorrelation stacks in the following frequency bands (Hz); [0.3–1], [0.4–1], [0.5–1] and [0.5–2]. First, we analyse the reflectivity changes along the waveforms of the autocorrelation stacks by using visual inspection. Afterwards, we analyse the temporal stability of the stacking process by plotting all daily autocorrelations for the complete data set, which are compared to the final stacks. In addition, we analyse convergence to the final average for the winter and summer months separately, by calculating the correlation coefficient between cumulative and final stacks. Furthermore, we show the automatically picked arrival times of the Moho reflections in different frequency bands. At last, we plot the final autocorrelation stacks of the stations alongside the whole CIFALPS profile, together with the picked arrival times of the Moho reflections, which are scaled to two-way traveltime (TWT) and migrated to depth. The autocorrelated stacks are plotted from 5 s TWT, to avoid the dominance of the large pulses at and after 0 s.

3.1 Autocorrelation stacks and temporal stability

The autocorrelation stacks of station CT22 are shown in Figs 5(b)–(i) for the following frequency bands (Hz), respectively; [0.09–0.5], [0.1–0.5], [0.1–1], [0.3–1], [0.4–1], [0.5–1], [0.5–2] and [1–2]. The autocorrelation stacks filtered with cut-off frequency less than or equal to 0.1 Hz (Figs 5b–d) show signals with long periods and no clear reflection changes. Therefore, it is difficult to detect crust–mantle reflections in these frequency bands and they have been discarded from further analysis. The autocorrelation stack filtered between 1 and 2 Hz (Fig. 5i) shows no clear reflectivity changes. The autocorrelation stacks of CT22 that are highlighted by the red box (Figs 5e–h) show clearly visible changes in reflectivity along the waveforms and are selected for further analysis. The points of changes in reflectivity are marked by the green dashed–dotted lines. The prior Moho information by Zhao *et al.* (2015) is marked by the pink dashed–dotted line. In addition, the prior information of the intracrustal discontinuity by Zhao *et al.* (2015) of the upper to lower crust has also been marked by the red dashed–dotted line to investigate the possibility of associating the changes in reflectivity to the intracrustal discontinuity.

The first changes in reflectivity are associated with a clear decrease in amplitude after the green dashed–dotted line, which lies around 11 s TWT for the 0.3–1 Hz autocorrelation stack and around 8.5 s TWT for the [0.4–1], [0.5–1] and [0.5–2] Hz frequency bands. The 11 s TWT reflectivity change has a difference of around 4 s TWT with the *a priori* intracrustal arrival time, whereas for the 8.5 s TWT reflectivity change there is a close match with the prior intracrustal information with a difference of around 1 s TWT. Furthermore, the first reflectivity change at around 11 s TWT in the 0.3–1 Hz autocorrelation stack, Fig. 5(e), lies closer to the *a priori* Moho arrival time with a difference of around 2 s TWT than to the *a priori* intracrustal arrival time. Therefore, it becomes difficult to relate this change in reflectivity to a specific discontinuity. The second changes in the reflection pattern along the autocorrelation stacks, at around 14 s TWT, are associated with a clear increase in amplitude and they closely match the prior Moho information by Zhao *et al.* (2015). There is a third change in reflectivity at later arrival times, at around 20 s TWT, that are marked by a decrease in amplitude. For the autocorrelation stacks filtered in the [0.3–1] and [0.4–1] Hz frequency bands, Figs 5(e) and (f), the third reflectivity changes are also associated with a change in frequency. The second change in reflectivity may be related to the base of the crust–mantle transition and the third change in the reflectivity pattern to the end of the crust–mantle reflection phase.

In Figs 6(a)–(d) we plot all daily autocorrelation stacks for the complete data set of station CT22 for, respectively [0.3–1], [0.4–1], [0.5–1] and [0.5–2] Hz frequency bands, along with the sum of the daily stacks for each frequency band (labelled as 'Final stack' in the figure). This plot—that we produced and inspected for all stations—is important to assess the coherence of the daily averages that merge into the final sum. The daily autocorrelation stacks in the different frequency bands show overall good temporal stability. The [0.4–1], [0.5–1] and [0.5–2] Hz frequency bands have clear stable crustal reflectivity between 14 and 20 s TWT, outlined in green, which is less distinctive in the 0.3–1 Hz frequency band. In addition, these stable reflections along the daily stacks fall in between the second and third change of reflectivity that has been detected along the waveforms of the final autocorrelation stacks in Figs 5(f)–(h). The stable reflections between 14 and 20 s TWT may be less distinctive in the [0.3–1] Hz frequency band due to the longer wavelengths that are not able to detect the finer crustal boundaries. Furthermore, the [0.4–1] and [0.5–1] Hz frequency bands have at around 5–8 s TWT clear stable reflections that are absent in the [0.3–1] and [0.5–2] Hz frequency bands due to the waveforms between the daily autocorrelation stacks being less coherent.

We have further investigated the temporal stability by calculating the correlation coefficient between each daily stack and the final stack for the entire time interval of 5–35 s TWT. In addition, we also compute the correlation coefficient between the running accrued average of past daily stacks and the final total sum. Fig. 7(a) shows the time evolution of these correlation coefficients for station CT22 filtered in the 0.5–1 Hz frequency band and Fig. 7(b) shows all daily stacks and the final stack. The correlation coefficient between each single day and the final stack is shown by the blue line in Fig. 7(a) that displays quite strong oscillating variations along the time interval, denoting the cyclic presence of perturbed (with low correlation) and better days (with high correlation). However, after stacking only 1 month of data the correlation coefficient reaches a stable value, as seen looking at the red line in Fig. 7(a) that shows a monotonically increasing trend with time before reaching a clear convergence. The same amount of stacked autocorrelations is needed for the [0.4–1] and [0.5–2] Hz frequency bands in order to reach a stable correlation coefficient. This is not the case for the autocorrelation stacks filtered in the [0.3–1] Hz frequency band, which shows less distinctive stable reflections in Fig. 6(a), the correlation coefficient reaches stability only after 4.5 months of data.

We also calculate the stability and convergence separately for the summer and winter months (Figs 7c and d), to investigate the seasonal effects on the reflections of the ambient noise autocorrelations. The daily stacks and the final stack of the summer days are shown in Fig. 7(e) and the equivalent is shown for the winter days in Fig. 7(f). The correlation coefficients in Fig. 7(c) are calculated as before between one daily stack of the summer and the final stack of the daily summer stacks, Fig. 7(e). The same is done for

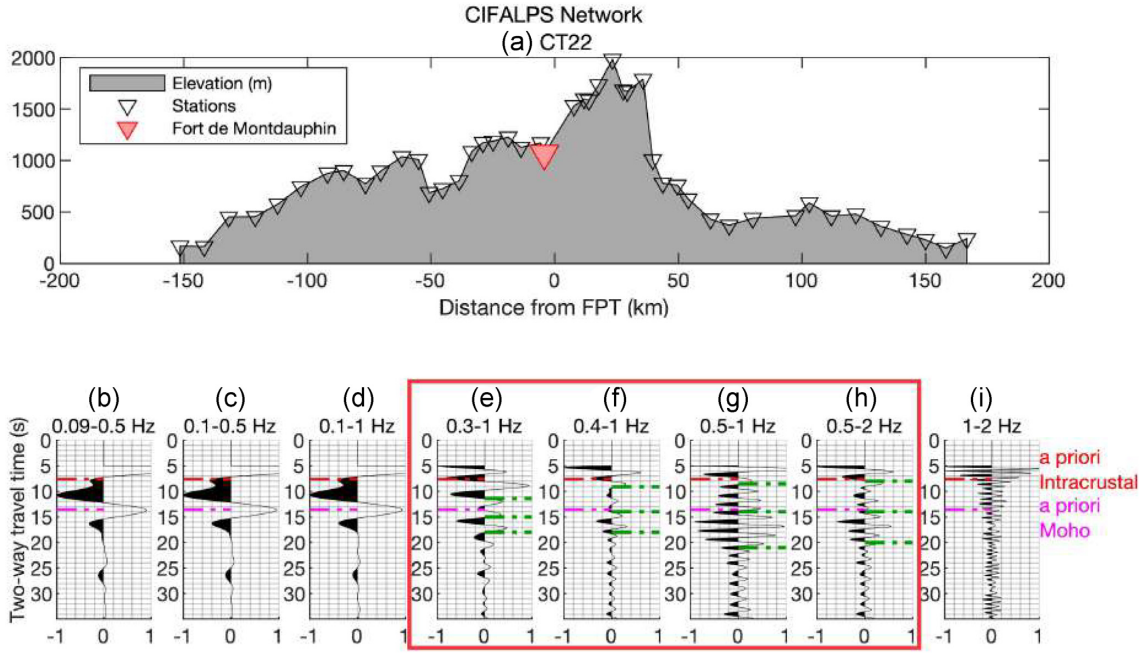

Figure 5. (a) Stations of the CIFALPS profile are plotted in elevation (m) from west to east. The position of Station CT22 is highlighted by the red upside down triangle. The autocorrelation stacks of station CT22 are shown in the following frequency bands (Hz); (b) [0.09–0.5], (c) [0.1–0.5], (d) [0.1–1], (e) [0.3–1], (f) [0.4–1], (g) [0.5–1], (h) [0.5–2] and (i) [1–2]. The autocorrelation stacks filtered with a cut-off frequency of ≤0.1 Hz show signals with long periods, leading to difficulties in detecting crustal reflections. No clear reflectivity change is visible in the 1–2 Hz frequency band. Therefore, the autocorrelation stacks in the red rectangle area are selected for further analysis. The previous intracrustal and Moho information by Zhao *et al.* (2015) are given by the red and pink dashed–dotted lines, respectively. The points where the reflection pattern changes along the waveforms of the stacks are marked by the green dashed–dotted line.

the winter months and are shown in Figs 7(d) and (f). The winter stack reaches a stable correlation coefficient value after just using less than half of the days of December, whereas the stack of the summer days reaches a strong correlation after one month which then suddenly decreases and reaches stability at a lower value. This decrease in stability, Fig. 7(c), can also be explained by the variance of the daily autocorrelation stacks. We calculate the amplitude variance of each correlogram for the entire time interval of 5–35 s TWT. Schimmel *et al.* (2021) have evaluated signal stability—used to compute autocorrelations—in connection to variability of noise root-mean squared amplitude, but we evaluate instead the variance of entire correlograms as a measure of complexity. Such variance clearly increases in the summer months (see Fig. S2). This increase may be associated with a decrease of natural sources during the summer months, such as the absence of winter storms, that may reasonably generate a more diffused noise field, that yield clearer autocorrelations. In addition, the mean variance of the summer months, Fig. S2(c), is higher than both the mean of the complete data set and the mean of only the winter months.

We marked the prior Moho and intracrustal arrival time along the waveform of the final summer and winter stack, Figs 7(e) and (f), together with the manually picked changes in reflectivity of Fig. 5(g). The striking outcome is that the manually picked changes in reflectivity are also associated with clearly visible reflectivity changes in the final winter stack, which is not the case for the final summer stack. The daily summer stacks show strong stable reflections, but they are hard to associate to a clear change in reflectivity along the final summer stack. Furthermore, the correlation coefficient between the final winter stack, Fig. 7(f), and the complete final stack, Fig. 7(b), has a value of 0.99 compared to the correlation coefficient of 0.93 between the final summer stack, Fig. 7(e), and the complete final stack. The final winter stack has a higher correlation with the complete final stack that may be due to the atmospherical winter storms that favour reaching stability faster.

3.2 Picked arrival times of the Moho reflectivity

For stations CT22 and CT15, Figs 8 and 9, we show the autocorrelation stacks along with the automatically picked changes in reflectivity, blue dashed–dotted line in the left plot, based on the prior Moho information by Zhao *et al.* (2015), pink dashed–dotted line. To investigate the possibility of associating the intracrustal discontinuity to the automatically picked reflectivity changes, we have also plotted the prior intracrustal information by Zhao *et al.* (2015) as a red dashed–dotted line. For each autocorrelation stack, the second derivative envelope is shown in the right-hand plot with the automatically picked reflectivity change (blue circle), which is based on the method by Becker & Knapmeyer-Endrun (2018). For each station we show the results in the following frequency bands (Hz): (a) [0.3–1], (b) [0.4–1], (c) [0.5–1] and (d) [0.5–2]. In the next paragraph, we analyse for each station separately the automatically picked changes in reflectivity that may be associated with the Moho reflectivity or the intracrustal discontinuity.

For station CT22, Fig. 8, the arrival times of the automatically picked reflectivity changes in the *a priori* time windows correspond to a clear change in reflectivity along the waveforms of the autocorrelations. Therefore, the arrival times of the automatically picked reflectivity changes are chosen as the arrival time of the Moho reflection and the intracrustal discontinuity. The automatically picked arrival times of the intracrustal discontinuity, are related to a clear decrease in amplitude along the waveforms of the autocorrelation stacks that are filtered in the [0.4–1], [0.5–1] and

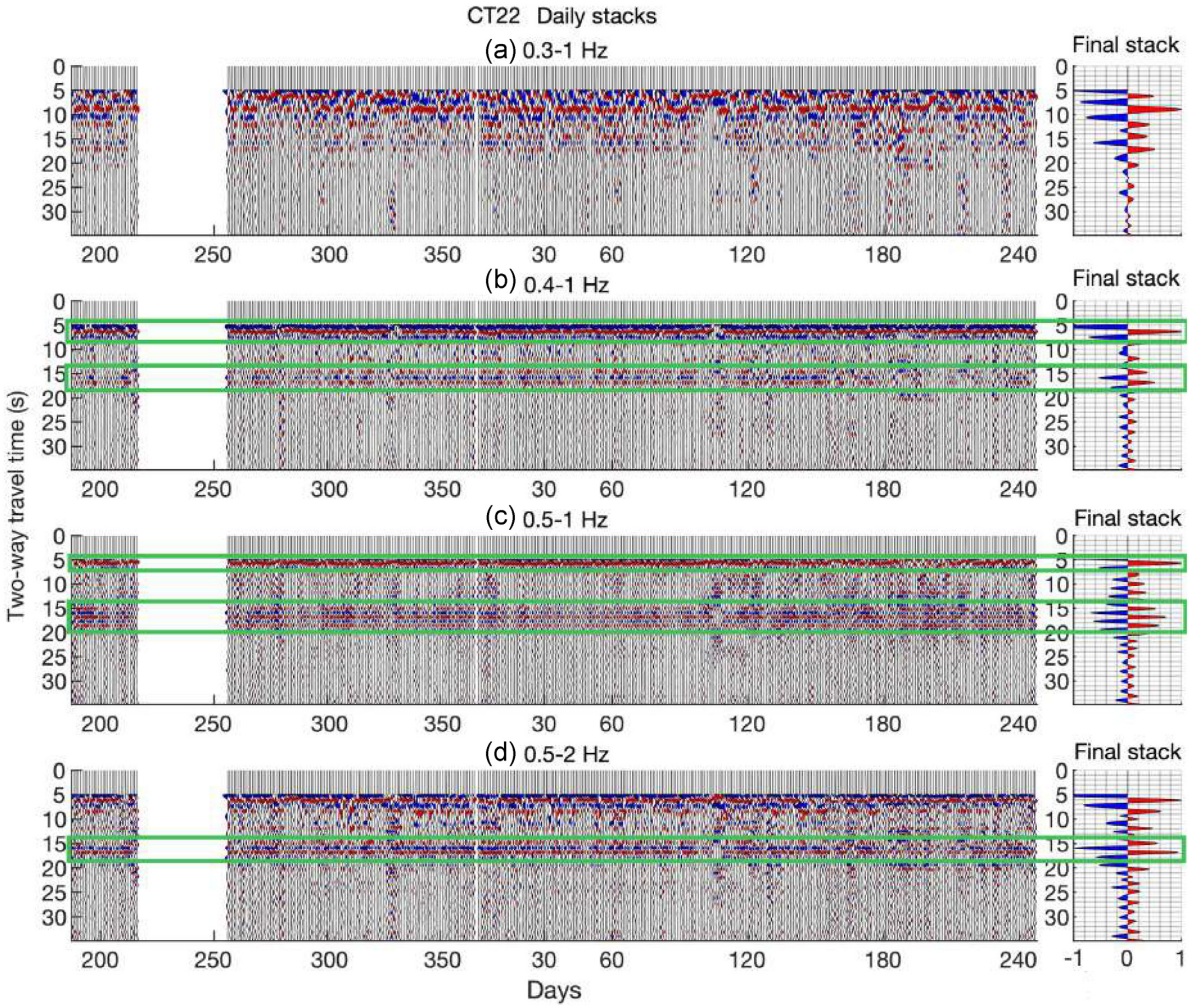

Figure 6. The daily autocorrelation stacks of station CT22 are filtered in the (a) [0.3–1], (b) [0.4–1], (c) [0.5–1] and (d) [0.5–2] Hz frequency bands. The final stack of the daily stacks in each frequency band are shown in the graph on the right-hand side. The areas outlined by the green rectangles, between ∼14 s TWT and ∼20 s TWT, are the distinctive stable reflectivities that may be due to the crust–mantle boundary. In addition, the stable reflectivities detected at earlier arrival times in the [0.4–1] and [0.5–1] Hz frequency bands may be due to the intracrustal discontinuity. The positive and negative amplitude lobes are filled with the red and blue colour, respectively.

[0.5–2] Hz frequency bands. However, in the [0.3–1] Hz frequency band the automatically picked arrival time of the intracrustal discontinuity is marked by an increase in amplitude that decreases shortly afterwards. The automatically picked arrival times of the Moho reflections are related to a clear increase in amplitude along the waveforms of the autocorrelation stacks that are filtered in all the four different frequency bands. These automatically picked reflectivity changes are very close—difference of ∼0.89 s TWT —to the manually picked changes in reflectivity, see Figs 5(e) to (h), except for the pick related to the intracrustal discontinuity in the [0.3–1] Hz frequency band that has a difference of ∼3.15 s TWT with the manual pick. Furthermore, the mean difference between the arrival times of the automatically picked reflectivity changes and prior information are ∼0.46 s TWT, which is smaller than the mean difference between the manually picked reflecitivity changes and prior information, ∼1.17 s TWT, that is mainly due to the manually picked arrival time of the intracrustal discontinuity at a much later time in the [0.3–1] Hz frequency band. The automatically picked reflectivity changes that are associated with the Moho reflections correspond to a clear peak in the *a priori* time window of the second derivative envelope for all the four different frequency bands.

For station CT15, the local maximum inside the *a priori* time window of the second derivative envelope in the 0.3–1 Hz frequency band (Fig. 9a) does not identify a single clear value. In addition, for the 0.5–1 Hz frequency band in Fig. 9(c) the local maximum is not the only clear peak in the *a priori* time window of the second derivative envelope. Therefore, in stations where the automatically picked arrival time of changes in reflectivity do not correspond to a single clear peak within the *a priori* time window, we associate the Moho reflection with the manually picked arrival time of the most stable reflection along the daily autocorrelation stacks that coincides with a clear change in reflectivity along the final autocorrelation stack. Fig. 9(e) shows the daily autocorrelation stacks filtered in the 0.5–1 Hz frequency band together with the manually picked arrival time, green dashed line, at the most stable reflection that coincides with a strong increase in amplitude after the pick along the waveform of the final stack. To have a clear view of the daily stacks, the green dashed line is plotted starting from the middle of the daily plots.

In Figs 9(a)–(d), we have only plotted the a prior time window of the prior Moho information due to the overlap with the *a priori* time window of the intracrustal discontinuity. The *a priori* time windows

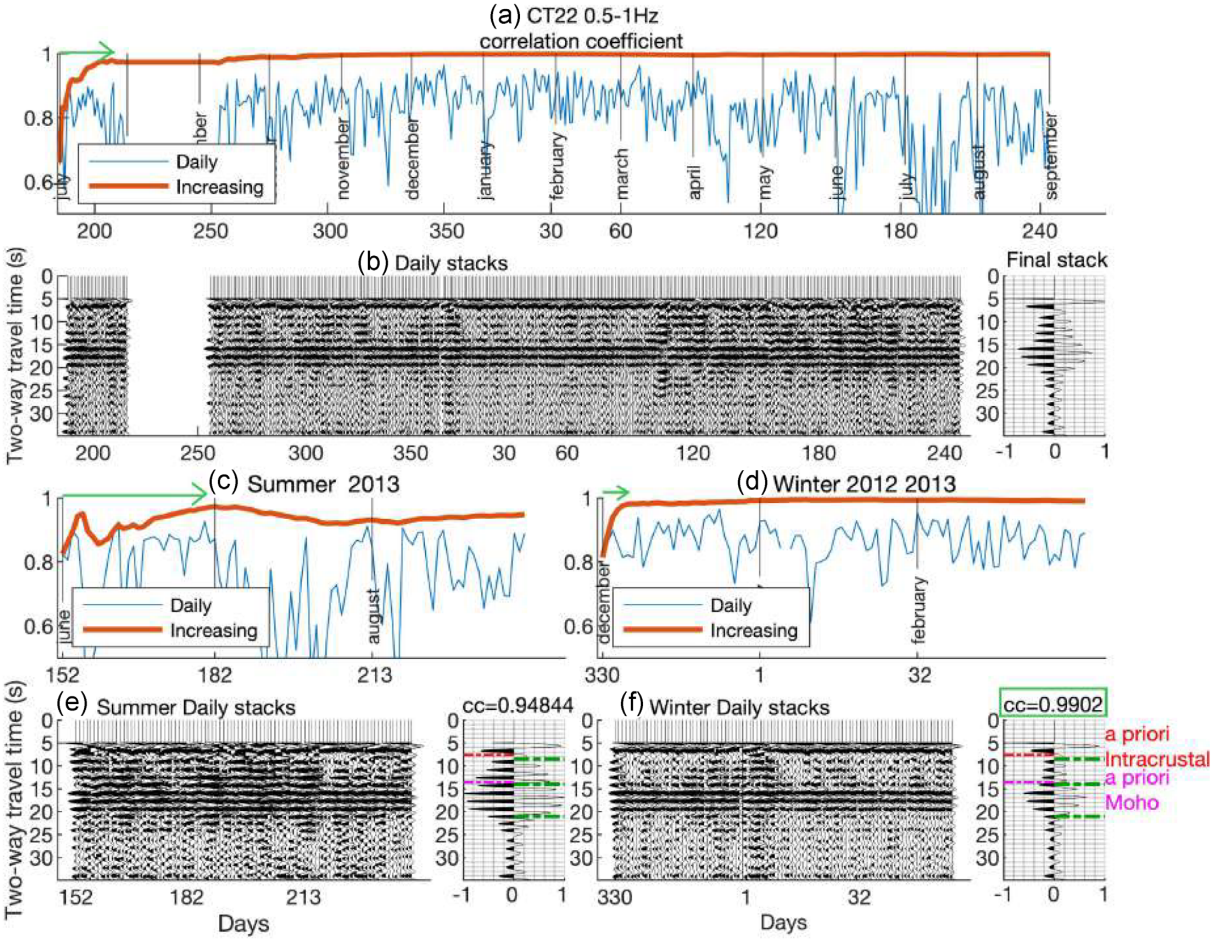

Figure 7. (a) The correlation coefficient for station CT22 filtered in the 0.5–1 Hz frequency band between the daily autocorrelation stacks and final stack shown in (b). The correlation coefficient between one day and the final stack is shown by the blue line. The red line is the correlation coefficient between stacked number of daily autocorrelations, that is increasing along with the operation time, and the final stack. The same procedure has been done separately for the summer months (c) and winter months (d). The daily stacks and final stack for the summer and winter are shown respectively in (e) and (f). The correlation coefficient between the final winter stack and the complete final stack shown in (b), given by the value cc, is marked by a green box due to the higher correlation as compared to the correlation coefficient value between the final summer stack and complete final stack. In addition, the prior Moho and intracrustal arrival time derived from Zhao *et al.* (2015) are plotted as a pink and red dashed–dotted line, respectively. The changes in reflectivity detected along the waveform of the final stack, see Fig. 5(g), are marked by the green dashed–dotted lines.

overlap when the difference between the prior Moho and intracrustal discontinuity is smaller than 5 s TWT. We also show the overlap of the *a priori* time windows in Fig. 9(f) with the automatically picked changes in reflectivity. The local maximum that is associated with the intracrustal discontinuity is at the border of the *a priori* time window. In addition, this local maximum falls inside the *a priori* time window that is related to the prior Moho information and very close to the manually picked change in reflectivity, green dashed–dotted line, that is selected as the Moho reflection.

3.3 Moho reflectivity across the CIFALPS profile

After picking the arrival times of the Moho reflections, we plot these arrival times with the final autocorrelation stacks of the stations alongside the reference profile (see Fig. 1) to image possible lithospheric structures and the Moho discontinuity. In Fig. 10(a) the altitude profile of the stations are plotted across the whole CIFALPS transect from west to east, and for each station the autocorrelation stacks filtered in the 0.5–1 Hz frequency band are plotted in the reflectivity profile, Fig. 10(b). The autocorrelations and automatically picked arrival times are in two-way traveltime (s) and stacked over the complete data set. The autocorrelation stacks filtered in the 0.5–1 Hz frequency band have been chosen for the reflectivity profile across the CIFALPS transect due to the clear reflectivity changes along the waveforms of the autocorrelation stacks. The reflections of the stations CT30–CT36 are dominated by a repeated 1 Hz signal throughout the stack. After analysing the probability power spectral densities—see Fig. S3—we exclude the frequency of 1 Hz and create autocorrelation stacks with a lower cut-off frequency of 0.3 Hz frequency. The 1 Hz signal may be due to instrumental problems since at this specific frequency there is very little variance in the power density spectrum. For further analysis of the reflectivity profile across the CIFALPS transect, we have replaced the autocorrelation stacks of stations CT30–CT36 with the stacks filtered in the 0.3–0.9 Hz frequency band (Fig. 10c) due to the improved reflection responses and clear reflectivity changes after the picked arrival times of the Moho reflections. In Fig. 10(c) the manually picked arrival times of the Moho reflections, green short horizontal

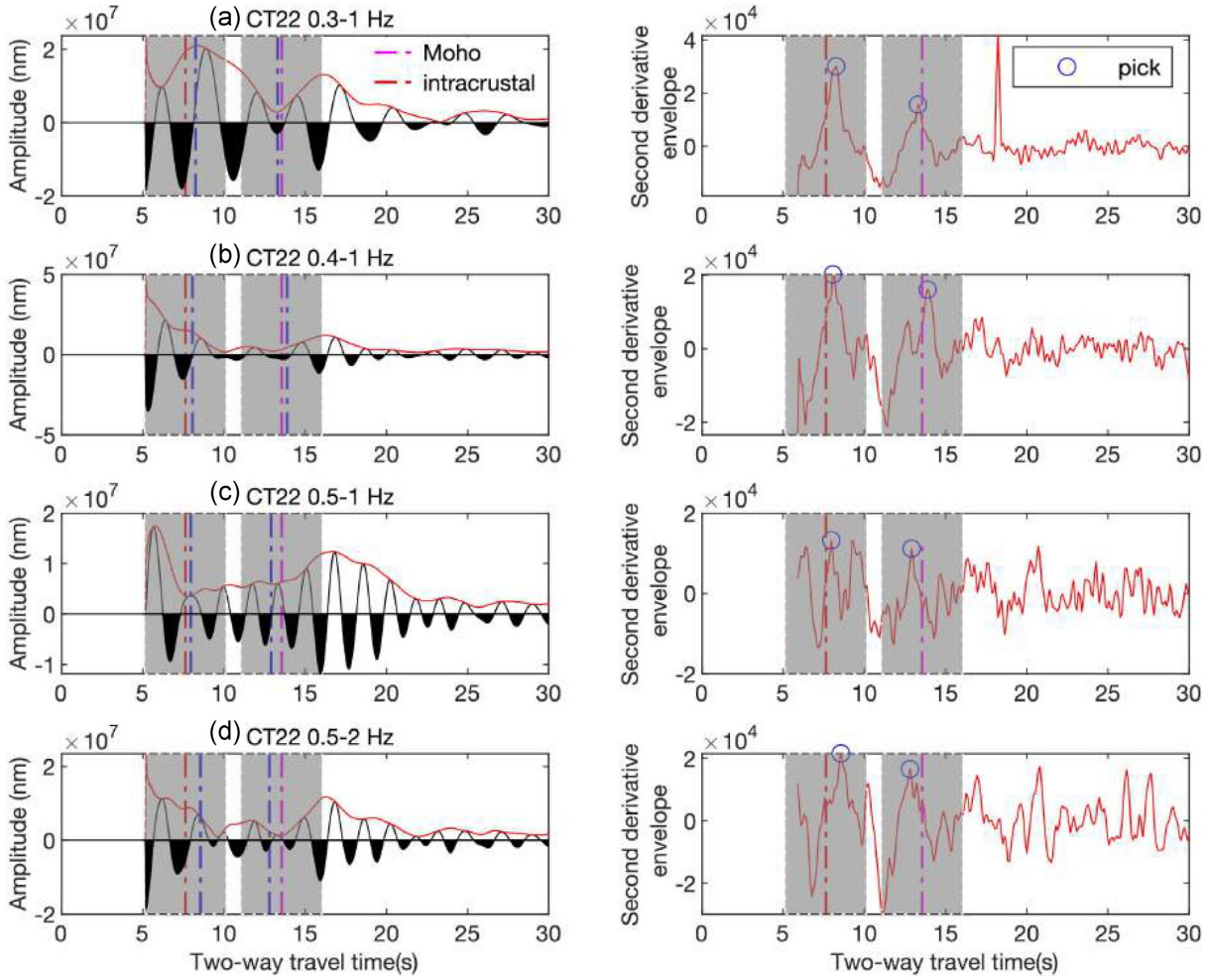

Figure 8. Plots on the left: the final autocorrelation stacks of station CT22 after processing the complete data set filtered in the following frequency bands (Hz); (a) [0.3–1], (b) [0.4–1], (c) [0.5–1] and (d) [0.5–2] with the arrival times of the automatically picked reflectivity changes, blue dashed–dotted lines, related to the Moho discontinuity and intracrustal discontinuity. The envelope of the autocorrelation stack is the red line. Plots on the right-hand side: the second derivative of the envelope with the picked reflectivity changes or local maxima, blue circles, inside the *a priori* time windows, grey windows. The prior Moho information by Zhao *et al.* (2015) is the pink dashed–dotted line and the red dashed–dotted line is the prior intracrustal information by Zhao *et al.* (2015).

lines, are selected for calculation of the Moho depth for the stations where the automatically picked arrival times did not correspond to a clear peak in the *a priori* time window of the second derivative envelope.

In Fig. 10(d) the reflectivity profile and the arrival times of the Moho reflections are converted into depth (km), using the velocity model by Zhao *et al.* (2015), and corrected for elevation. There is some spatial coherence at ∼18–23 km depth between the waveforms of the autocorrelation stacks of different stations from the beginning of the CIFALPS line, –150 km from the Frontal Penninic thrust (FPT—0 km), to –70 km and from –30 to 30 km after the FPT. Coherence then disappears into strong lateral variations towards the eastern end of the profile. Furthermore, from –150 to –100 km from the FPT the reflectivity fades after the Moho reflections, due to a clear decrease in amplitude along the waveforms of the autocorrelation stacks. However, from –100 km to the FPT there is vertical continuity of reflectivity down to 75 km depth and in between the stations there is weak spatial coherence. The Moho reflections in the eastern part of the profile line, 100–170 km after the FPT, are shallower than in the western part, –150 to 50 km after the FPT. The deepest Moho reflections are at the stations CT30 and CT31, at a depth of around 70 km.

We have also picked the Moho reflections manually for the stations where the automatic method corresponded to a single clear peak within the *a priori* time window of the second derivative envelope. The depth of the manually picked Moho reflections are shown together with the outline of the geological cross-section by Zhao *et al.* (2015, see Fig. S4). The mean difference between the depth of the manually picked Moho reflections and the depth by Zhao *et al.* (2015) is 1.1 ± 1.3 km. The Moho depths from the manually picked reflections are mostly deeper beneath the western end of the profile, –75 km to the FPT, than the study by Zhao *et al.* (2015). The mean difference between the depth of the automatically picked Moho reflections and the depth by Zhao *et al.* (2015) is -1.8 ± 0.9 km. The Moho depths from the automatically picked reflections are mostly shallower than the study by Zhao *et al.* (2015, see Fig. S4c). For each station, the difference between the Moho depth from manual picking and the Moho depth obtained from the automatic method is shown in Fig. S4(d). There are large differences at the beginning of the line, the middle of the western end of the profile, –75 to –10 km from the FPT, and at the start of the subduction zone, 30–50 km after the FPT. The mean difference between the Moho depth from manual picking and Moho depth from the automatic method is 2.8 ± 1.8 km.

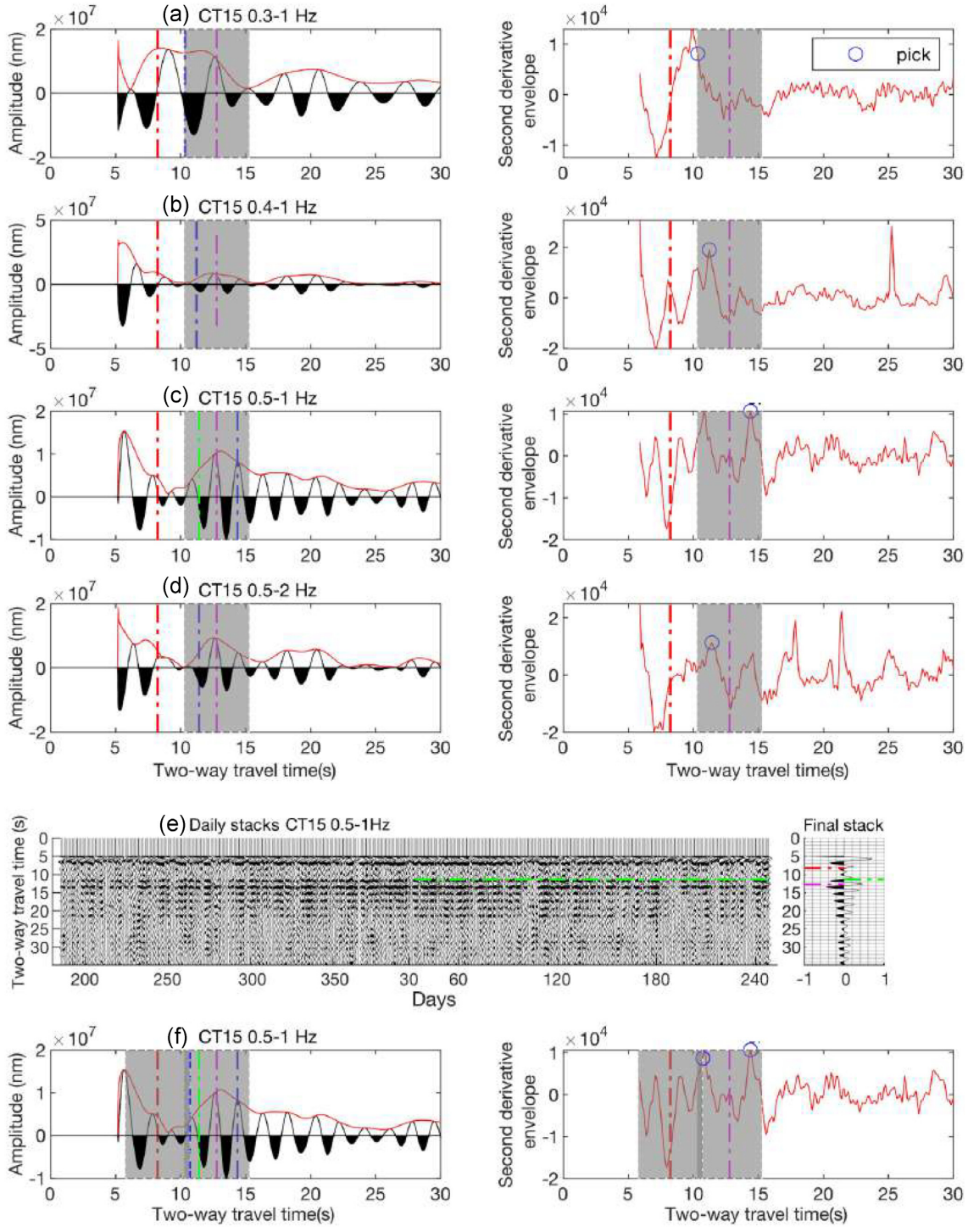

Figure 9. Plots on the left: the final autocorrelation stacks of station CT15 after processing the complete data set filtered in the following frequency bands (Hz); (a) [0.3–1], (b) [0.4–1], (c) [0.5–1] and (d) [0.5–2] with the arrival times of the automatically picked reflectivity changes, blue dashed–dotted lines, related to the Moho discontinuity and (f) intracrustal discontinuity. The envelope of the autocorrelation stack is the red line. Plots on the right-hand side: the second derivative of the envelope with the picked reflectivity changes or local maxima, blue circles, inside the *a priori* time windows, grey windows. The prior Moho information by Zhao *et al.* (2015) is the pink dashed–dotted line and the red dashed–dotted line is the prior intracrustal information by Zhao *et al.* (2015). The manually picked arrival time associated with the Moho reflection is shown by the green dotted line in (c) at the most stable reflection along the daily stacks (e) and coincides with a clear change in reflectivity along the waveform of the final stack. (f) The automatically picked arrival time of the intracrustal discontinuity is close to the manually picked arrival time of the Moho reflection as opposed to the prior intracrustal information by Zhao *et al.* (2015).

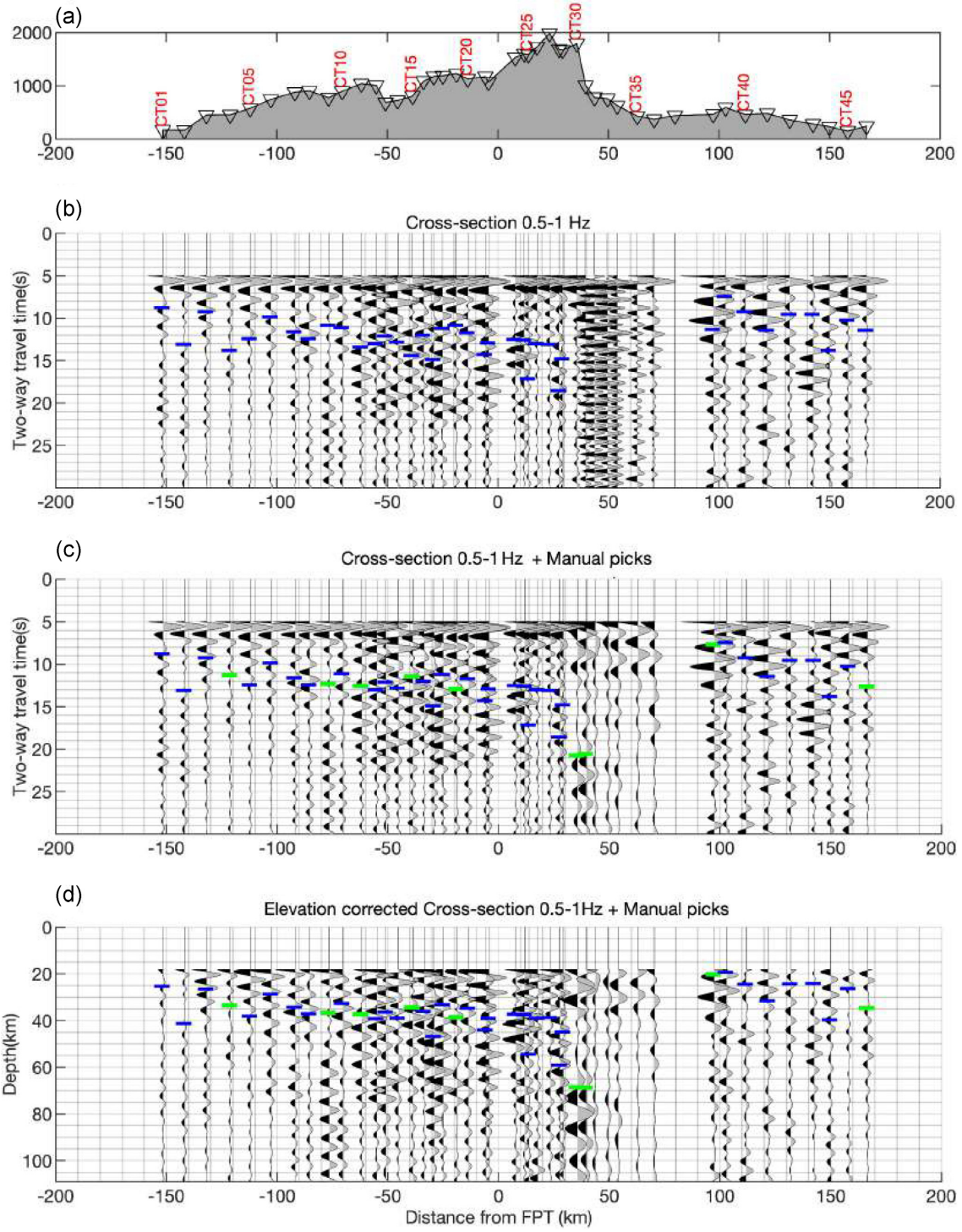

Figure 10. (a) Altitude profile in metres for the CIFALPS transect from west to east. Stations are shown by the inverted triangles; labels in red represent the station codes. The distance is measured from the Frontal Penninic Thrust (FPT) show in Fig. 1. (b) The autocorrelation stacks in the 0.5–1 Hz frequency band of the CIFALPS stations are plotted in two-way traveltime, with the arrival times of the automatically picked reflectivity changes that are related to the Moho reflection, blue short horizontal lines. (c) The stacks of stations CT30–CT36 are replaced with the 0.3–0.9 Hz autocorrelation stacks due to the improved reflection response after excluding the 1 Hz signal. The automatically picked arrival times that do not correspond to a clear change in reflectivity along the waveforms of the autocorrelation stacks are replaced by the arrival times of the most stable reflection that are chosen as the Moho reflection, green short horizontal lines. (d) The autocorrelation reflectivity profile and the arrival times of the Moho reflection are migrated to depth (km), and corrected for elevation, using the velocity model by Zhao *et al.* (2015).

4 DISCUSSION

The main goal of this study is to image the reflectivity of the crust–mantle boundary, and where possible detect reflectivity structures of the lithosphere, from autocorrelations of ambient seismic noise along the CIFALPS profile. Autocorrelation stacks for all the stations show indication of a gradational, as opposed to sharp, Moho interface because of the absence of a corresponding dominant pulse. In this case it is helpful to identify the Moho based on prior information (e.g. Kennett *et al.* 2015; Becker & Knapmeyer-Endrun 2018). Therefore, the method of Becker & Knapmeyer-Endrun (2018) that is based on prior information is a helpful tool to pick the reflectivity changes that are associated with the Moho discontinuity. We have only used the prior information by Zhao *et al.* (2015) due to the well-defined final crustal model that aid in the interpretation of the autocorrelation reflectivity profile.

In Fig. S5, we use the Moho from the ambient noise tomography study by Lu *et al.* (2018) to investigate the effect on picking the arrival time of the Moho reflection with a different prior information. The study by Lu *et al.* (2018) resulted into a shallower Moho depth of 5–8 km at the western end of the profile, beneath the Southeast Basin, than the study by Zhao *et al.* (2015). In other areas along the profile it is in good agreement with Zhao *et al.* (2015). Therefore, we have selected station CT01 that is positioned at the western end of the profile where the Moho from Zhao *et al.* (2015) and Lu *et al.* (2018) have the largest difference, ∼8 km. The local maximum inside the priori time window of the second derivative envelope is the same peak with the same arrival time (see Fig. S5) for using the prior Moho by; (a) Zhao *et al.* (2015), (b) Lu *et al.* (2018) or (c) average of the aforementioned prior Moho. This shows that the picked arrival times of the Moho reflections, for stations where previous studies resulted in large Moho depth differences, are robust since the arrival time stays the same when using a different prior Moho.

The reflectivity changes are automatically picked inside *a priori* time window set at a length of 5 s TWT that is around 18 km and is not defined by uncertainties of the prior Moho information or velocity model by Zhao *et al.* (2015) since these values are not available. In the study by Becker & Knapmeyer-Endrun (2018), the arrival time of the Moho reflections across the Trans-European Suture Zone are picked inside *a priori* time windows that vary based on the uncertainties of the selected prior Moho and velocity model. Their prior time windows generally resulted in shorter windows, < 5 s TWT. However with the larger *a priori* time window that is fixed at 5 s TWT, we take into consideration more changes in reflectivity that may be associated with the Moho reflection and the results are less biased to the uncertainties of the prior information. Furthermore, the manually picked arrival times of the Moho reflections are not confined to a fixed *a priori* time window. This results in a maximum of ∼1.4 s TWT, which is at station CT30, outside the *a priori* time window.

We have shown that by stacking only the daily autocorrelations of the winter months in the time interval of 5–35 s TWT (Fig. 7f), the final winter stack is very similar to the final stack of the complete data set with a correlation coefficient of 0.99. The winter daily stacks reach stability faster, most likely because of the winter storms resulting in a more diffuse and stable noise field, and hence more stable *P*-wave reflection signals. In a very different environment, Schimmel *et al.* (2021) have shown that autocorrelation convergence speed generally worsen with increasing lag time. In our data, we observe that convergence is faster for the whole correlogram in winter as opposed to summer. Weaker generation of ambient noise may therefore lead to a general increase of variance in the broad lag time window.

The choice of frequency band is very important as we can see from the results of Figs 6, 8 and 9. In Fig. 6 the waveforms of the daily autocorrelation stacks filtered in the [0.3–1] and [0.5–2] Hz frequency bands are less coherent than the daily stacks filtered in the [0.4–1] and [0.5–1] Hz frequency bands. The coherence between the waveforms of the daily stacks is important since the manually picked arrival time of the Moho reflection is associated with the most stable reflection along the daily stacks that coincides with a clear change in reflectivity along the final autocorrelation stack. In Figs 8 and 9, the arrival time of the automatically picked reflectivity changes are associated with a clear change in amplitude along the waveforms of the autocorrelations that are filtered in the 0.5–1 Hz frequency band. The change in amplitude is also visible in the 0.4–1 Hz frequency band, but not as notable. Therefore, we have chosen the seismograms that are filtered in the 0.5–1 Hz frequency band, as we observe a clear change in reflectivity after the picked arrival times of the Moho reflections due to the transition between the crust and mantle.

Below 1 Hz, the dominant source of the ambient seismic wavefield is oceanic gravity waves. The 0.5–1 Hz frequency band is within the secondary microseisms range (0.1–1 Hz) whose excitation sources are distributed in both shallow, coastal areas and pelagic areas (Nishida 2017). Above 1 Hz, the dominant source of the wavefield is human activities (Bonnefoy-Claudet *et al.* 2006). In the 0.5–2 Hz frequency band, the wavefield is excited by both oceanic gravity waves, below 1 Hz, and human activities, above 1 Hz. At frequencies higher than 1 Hz, seismic noise systematically exhibits daily and weekly variations linked to human activities. These human activities that change on a daily base may explain the high variance observed between the daily stacks in the 0.5–2 Hz frequency band (Fig. 6d).

In contrast to our best results in the 0.5–1 Hz frequeny band, the studies by Becker & Knapmeyer-Endrun (2018) and Becker & Knapmeyer-Endrun (2019a) show best results in the 1–2 Hz range. The chosen frequency range may be different due to the different characteristics of the seismic station sites, and the noise field. The stations in this study are situated near the Ligurian Sea while those of Becker & Knapmeyer-Endrun (2018) near the Baltic Sea, two very different geological environments. A further study on the effects of ambient seismic noise level from different sea regions and site characters can give more insight on the best frequency window range.

In addition to the different chosen frequency ranges, different types of processing might influence the waveform of the final stack due to the signal and noise characteristics (Schimmel 1999). We have applied a classical autocorrelation with amplitude normalization by using 1-bit time-domain normalization whereas Becker & Knapmeyer-Endrun (2018) has used the phase autocorrelation method by Schimmel (1999). Schimmel *et al.* (2018) have shown that for the extraction of Earth orbiting surface waves from vertical-component seismograms the waveform of the amplitude unbiased phase autocorrelation stacks closely matches to the classical autocorrelation that uses amplitude normalized data. However, the same results were not achieved for the autocorrelation stacks filtered in a higher frequency band that might have been due to the quantity of the data used for the final stack. Therefore, there might be an influence of different processing steps. Nevertheless, more research can be done to give insight on how different processing steps behave in different frequency bands and on the extraction of Moho reflected *P* waves.

In this study we can observe layers starting from around 18 km, Fig. 10(d), since the autocorrelated stacks are plotted from 5 s TWT, to avoid the dominance of the large pulses at and after 0 s. To estimate the vertical resolution of the reflectivity profile in the the 0.5–1 Hz frequency band, we take into consideration the general threshold of $\lambda/4$ (e.g. Yilmaz 2001). In the upper crust along the CIFALPS profile, the seismic wavelength ranges from 6 km for the 1 Hz seismic wave to 12 km for the 0.5 Hz seismic wave. The 6 km wavelength can observe an upper crust down to 1.5 km thick, whereas the 12 km wavelength can observe a minimum thickness of 3 km. In the lower crust the wavelengths are ranging from 6.6 to 13.2 km and the minimum resolvable layer thickness ranges between 1.65 and 3.3 km. The minimum thickness of the upper and lower crust are ∼4 and ∼6.6 km (Zhao *et al.* 2015), respectively, so even with the longer wavelengths of the 0.5 Hz frequency wave the interfaces of the upper and lower crust may be resolved. To improve the vertical resolution and resolve layers that are shallower than 18 km, including higher frequency waves may be of great importance.

We have not applied Automatic Gain Control (AGC), that is commonly used in exploration seismology, since the method of Becker & Knapmeyer-Endrun (2018), that we also use here, is based on picking reflectivity changes. The reflectivity changes that we have observed in Figs 5, 8 and 9 are mainly associated with changes in amplitude. AGC increases the amplitude levels of weak signals. In our study, the changes in amplitude are important to detect reflectivity changes that are associated with the Moho interface. Therefore, we leave the character of the autocorrelations in its original state.

In Fig. 11, we compare the Moho depths calculated from the arrival times of the picked reflectivity changes along the autocorrelation stacks in the 0.5–1 Hz frequency band to the structure of the geological cross section by Zhao *et al.* (2015). This comparison aids also in interpreting the different characters observed along the reflectivity profile, marked by cyan–green outlines from (1) to (4). The eastward dipping subduction trend of the European Moho going underneath the Adriatic Moho can clearly be followed with the Moho depths obtained in this study. From –150 to 30 km from the FPT, the Moho depths of this study are mostly shallower than the receiver function study by Zhao *et al.* (2015) and matches more closely to the Moho depths estimated by Lu *et al.* (2018). The earlier Moho arrivals in the eastern part of the cross section are related to the shallow depths of the Adriatic Moho. These shallow Moho depths have also been detected in the Moho maps by Lu *et al.* (2018) from surface wave tomography. The spatial coherence in the western part of the profile between ∼18 and 23 km depth, marked by the cyan–green lines (1) in Fig. 11(c), falls within the relatively homogenous crustal structure by Zhao *et al.* (2015). This homogenous behaviour has also been detected in the shear wave velocity models by Lyu *et al.* (2017). The coherence at these shallow depths after conversion of the time domain reflectivity profile starting from 5 s TWT, is unlikely to be influenced by the zero-lag sidelobes. The sidelobes wavelength are highly dependent on the frequency bandwidth: Romero & Schimmel (2018) have shown that the sidelobes are longer and arrive at later lag times for the frequency bands with a lower cut-off frequency. In our study, the effect of the zero-lag sidelobes from 5 s TWT has been discarded since the coherence detected between the waveforms of the daily autocorrelation stacks at early arrival times in the 0.5–1 Hz frequency band, Fig. 6(c), is not detected in the 0.3–1 Hz frequency band, Fig. 6(a), that would otherwise also show coherence but with longer wavelengths if there were influence from the zero-lag sidelobes.

The deeper reflections after the Moho reflections, marked by the cyan–green ellipse (2) in Fig. 11(c), from –100 km to the FPT along the CIFALPS profile fall right below the fault zone underneath the Southeast basin. The high amplitudes of these reflections were observable at stations in or near the fault zone, but not at stations further away. Li *et al.* (2007) demonstrated that the boundaries of fault zones create multiple reflections on synthetic seismograms. In addition, Lai *et al.* (2010) detected fault-zone trapped waves caused by multiple reflections between two boundaries of the fault and the wave interference. Whereas, Taylor *et al.* (2016) detected reduced reflectivity of the crustal–mantle boundary in the autocorrelations near the North Anatolian Fault zone fault. In our study, the Moho will not be affected by reduced reflectivity since the crustal–mantle boundary is based on the highest change of the slope in the envelope. So the deeper reflections detected in this study after the Moho reflection may be related to multiple reflections inside the fault zone. They cannot be related to deeper layers since there is no evidence of such layers in this study area. Furthermore, Kennett (2015) and Becker & Knapmeyer-Endrun (2019a) concluded that associations of deeper arrivals to asthenospheric depths is questionable since contaminations from shallow structures might influence those arrivals. Another study by Tibuleac & von Seggern (2012) associated deeper arrivals to Moho-reflected-*S* waves since there is no support of deeper layers from previous studies in their study area. However, we are considering to create synthetic autocorrelations in a further study to give more insight on these arrivals.

The highly reflective Moho along the CIFALPS becomes suddenly transparent to seismic waves between 50 and 100 km from the FPT, marked by the cyan–green circle (3) in Fig. 11(d). The reflection-free, transparent area falls within the position of the Ivrea body by Zhao *et al.* (2015). The Ivrea body is a high density and high-velocity body that reaches crustal depths as a slice of serpentinized Adriatic upper mantle (Closs & Labrouste 1963; Nicolas *et al.* 1990). The reflective transparency might be due to the presence of upper-mantle material at shallow depths, which has also been detected by the active seismic study of Nicolas *et al.* (1990). The ambient noise of the stations in the reflective transparent area have for the frequency range of 0.3–1 Hz the same level, ∼–150 to –120 dB, and follow the same trend as compared to stations outside this area (see Fig. S6). Therefore, it is most unlikely that the transparency of the seismic reflection might be due to different ambient noise levels.

Furthermore, the lateral variations observed towards the eastern end of the profile has also been observed in the v_S velocity models by Lyu *et al.* (2017) that shows strong lateral variations and very high velocities of lithospheric mantle beneath the Po plain with very low velocities at the deeper parts. The deepest Moho reflections at the stations CT30 and CT31 are ∼70 km, and ∼15 km deeper than the prior Moho depth of ∼55 km by Zhao *et al.* (2015) underneath the same stations. The extent of the Moho that is marked by the cyan–green line (4) in Fig. 11(d) follows a steeper trend compared to the prior Moho profile by Zhao *et al.* (2015) and Lyu *et al.* (2017). The shape of the Moho shows a clear steeper dip from ∼55 to ∼70 km.

Associating the Moho reflection to the most stable reflection along the daily autocorrelation stacks without prior information might result into picking a stable reflection from another discontinuity. In Fig. 9(e) there is a stable reflection along the daily stacks, at ∼7 s TWT, that is associated with a clear change in reflectivity along the final stack and very close to the intracrustal discontinuity obtained from Zhao *et al.* (2015), at ∼8 s TWT. Furthermore, the Moho depths obtained from picking manually the most stable reflections along the daily autocorrelation stacks (Fig. S4b)

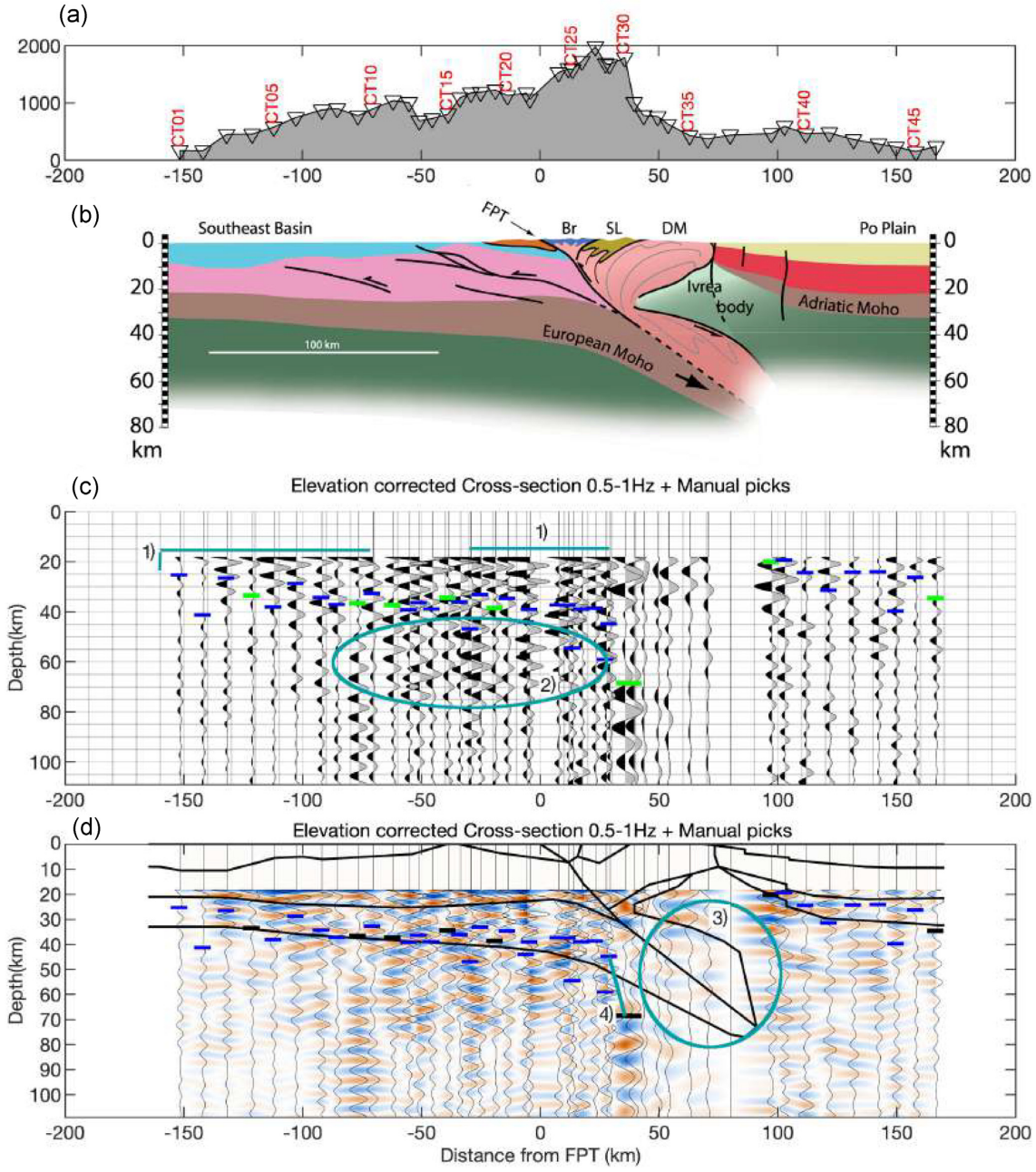

Figure 11. (a) Altitude profile in metres of the CIFALPS stations from west to east, the distance is given from the Frontal Penninic Thrust (FPT) show in Fig. 1. (b) The geological cross-section from the receiver function study by Zhao *et al.* (2015). (c) The autocorrelation reflectivity profile plotted in depth (km) after correcting for elevation. The Moho depths calculated from the arrival times of the automatically picked reflectivity changes are given by the blue short horizontal lines and the depths of the Moho reflections from manual picking by the green and black short horizontal lines in (d). The velocity model by Zhao *et al.* (2015) has been used. The spatial coherence in the western part of the profile, marked by the cyan–green lines (1), coincide with the relatively homogeneous crustal structure. In addition, the deeper reflections after the depths of the Moho reflections that are marked by the cyan–green circle (2) might be the multiple reflections due to the fault zone. See text for further explanation. (d) The autocorrelation stacks are plotted on the image view created from the reflections. The positive lobes are plotted on top of the red colour and the negative lobes on top of the blue colour. The outline, thick black lines, of the geological cross-section in (b) are plotted on top of the reflection profile. The cyan–green circle (3) highlights the transparent reflectivity profile and might be due to the effect of the Ivrea Body. The steep extent of the Moho is marked by the cyan–green line (4). See text for further explanation.

resulted mostly deeper in the middle of the CIFALPS profile, –70 to –10km from the FPT, than the results from the automatic method and prior information by Zhao *et al.* (2015). These results might be biased due to the stable multiple reflections, from the fault zone area underneath the Southeast basin, that are arriving at later times. The method of Becker & Knapmeyer-Endrun (2018) that is based on prior information to extract the largest changes in the slope of the envelope has proven to not be affected by the deeper reflections or by stable reflections from the intracrustal discontinuity.

In addition to picking the arrival times associated with the Moho reflection, we apply the automated picking method by Becker &

Knapmeyer-Endrun (2018) to investigate the possibility of detecting the intracrustal discontinuity. For station CT22, the automatically picked arrival time of the intracrustal discontinuity is clearly separated from the arrival time of the Moho discontinuity. This is not the case for station CT15, Fig. 9(f), where the automatically picked arrival time of the intracrustal discontinuity is very close to the reflectivity change associated with the Moho reflection. Another outcome is that the automatically picked arrival time of the intracrustal discontinuity corresponds to the same peak that is associated with the reflectivity change of the Moho discontinuity, and thus at the same arrival time, see Fig. S5(d) for station CT01. The automatically picked arrival time closely matches the shallower Moho information by Lu *et al.* (2018), Fig. S5(b). Shortening the *a priori* time windows may solve the problem but would not exclude the possibility that the arrival time of the automatically picked change in reflectivity related to the intracrustal discontinuity might be associated with a deeper discontinuity.

The seismic *P*-wave velocity changes across the intracrustal and Moho discontinuity might give insight on the character of the reflectivity changes or local maxima inside the *a priori* time window of the second derivative envelope when the two discontinuities lie close to each other. The *P*-wave velocity model of Zhao *et al.* (2015) increases from 6.0 to 6.6 km s^{-1} for the upper to lower crust, intracrustal discontinuity and from 6.6 to 8.2 km s^{-1} for the lower crust to mantle, Moho discontinuity. The velocity change for the intracrustal discontinuity is not as large as the Moho discontinuity. These different velocity changes might result into the peak of the reflectivity change associated with the intracrustal discontinuity being lower than the peak of the Moho discontinuity. This higher peak of the Moho discontinuity outweighs the lower peak of the intracrustal discontinuity when picking the local maximum inside the *a priori* time window. Therefore, when two discontinuities are close to each other the discontinuity with the smaller velocity change might be biased by the discontinuity with a larger change in velocity that creates a higher peak inside the *a priori* time window of the second derivative envelope. A further study needs to be done on how the reflectivity change of the intracrustal discontinuity is affected by the reflectivity change of the Moho discontinuity when they lie close to each other.

5 CONCLUSIONS

We show that ambient noise autocorrelations coherently image the reflectivity structure of the crust–mantle boundary, and thus clearly depict the subduction of the European plate underneath the Adriatic micro plate. We have created autocorrelations in the [0.09–0.5], [0.1–0.5], [0.1–1], [0.3–1], [0.4–1], [0.5–1], [0.5–2] and [1–2] Hz frequency band by stacking hourly segments over the complete data set of the CIFALPS. The effects from earthquakes and powerful events have been removed by applying sign-bit normalization (Bensen *et al.* 2007). We have picked the arrival time of the Moho reflection by automatically picking reflectivity changes (Becker & Knapmeyer-Endrun 2018) and using prior information from Zhao *et al.* (2015). The results are the best in the 0.5–1 Hz frequency band due to the clear change in reflectivity along the waveforms of the autocorrelation stacks after the arrival time of the Moho reflections. The dense station spacing of the CIFALPS makes it easy to detect the different geological structures along the autocorrelation reflectivity profile. The western part of the profile is characterized by spatial coherence at shallow arrivals, due to the homogenous crustal structure at shallow depths (Zhao *et al.* 2015). After the depth of the Moho reflections in the western part there is a zone with strong reflections, that are possibly due to the multiple reflections caused by the boundaries of the fault zone (Li *et al.* 2007). The eastern part of the profile is marked by a reflective transparent area due to the Ivrea body reaching shallow crustal depths (Closs & Labrouste 1963; Nicolas *et al.* 1990). The subduction profile of the European Plate shows a steep trend as compared to previous studies by Zhao *et al.* (2015) and Lyu *et al.* (2017). Our observations show the ability of mapping not only homogenous structures but also highly laterally heterogeneous structures.

ACKNOWLEDGEMENTS

We are very thankful to the anonymous reviewers and Irene Molinari for their constructive feedback which helped to improve this paper. We are also grateful to the operators of the French Seismologic and Geodetic Network for managing and making the data freely available at the Résif Seismological data portal.

DATA AVAILABILITY

The seismic data of the CIFALPS (Zhao *et al.* 2016) experiment is freely available at the Résif Seismological data portal (http://doi.org/10.17616/R37Q06). The seismic data are also archived at the data centre of the Seismic Array Laboratory, Institute of Geology and Geophysics, Chinese Academy of Sciences, and at the data centre of the French Seismologic and Geodetic Network.

REFERENCES

Asten, M., 1976. The use of microseisms in geophysical exploration, *PhD thesis*, Macquarie University, Sydney, Australia.

Becker, G. & Knapmeyer-Endrun, B., 2018. Crustal thickness across the trans-European suture zone from ambient noise autocorrelations, *Geophys. J. Int.,* **212**(2), 1237–1254.

Becker, G. & Knapmeyer-Endrun, B., 2019a. Crustal thickness from horizontal component seismic noise auto-and cross-correlations for stations in central and eastern Europe, *Geophys. J. Int.,* **218**(1), 429–445.

Becker, G. & Knapmeyer-Endrun, B., 2019b. Reply to 'Comment "Crustal thickness across the Trans-European Suture Zone from ambient noise autocorrelations" by G. Becker and B. Knapmeyer-Endrun' by G. Helffrich, *Geophys. J. Int.,* **217**(2), 1261–1266.

Beller, S., Monteiller, V., Operto, S., Nolet, G., Paul, A. & Zhao, L., 2018. Lithospheric architecture of the south-western Alps revealed by multi-parameter teleseismic full-waveform inversion, *Geophys. J. Int.,* **212**(2), 1369–1388.

Bensen, G., Ritzwoller, M., Barmin, M., Levshin, A., Lin, F., Moschetti, M., Shapiro, N. & Yang, Y., 2007. Processing seismic ambient noise data to obtain reliable broad-band surface wave dispersion measurements, *Geophys. J. Int.,* **169**(3), 1239–1260.

Bonnefoy-Claudet, S., Cotton, F. & Bard, P.-Y., 2006. The nature of noise wavefield and its applications for site effects studies: a literature review, *Earth-Sci. Rev.,* **79**(3–4), 205–227.

Claerbout, J.F., 1968. Synthesis of a layered medium from its acoustic transmission response, *Geophysics,* **33**(2), 264–269.

Closs, H. & Labrouste, Y., 1963. Recherches séismologiques dans les Alpes occidentales au moyen de grandes explosions en 1956, 1958 et 1960in *Mémoire Collectif du Groupe d'Études des Explosions Alpines,* Vol. **12,** CNRS.

Diehl, T., Husen, S., Kissling, E. & Deichmann, N., 2009. High-resolution 3-D P-wave model of the Alpine crust, *Geophys. J. Int.,* **179**(2), 1133–1147.

Gorbatov, A., Saygin, E. & Kennett, B., 2013. Crustal properties from seismic station autocorrelograms, *Geophys. J. Int.,* **192**(2), 861–870.

Grellet, B., Combes, P. & Granier, T., 1993. *Sismotectonique de la France métropolitaine dans son cadre géologique et géophysique: avec atlas de 23 cartes au 1/4 000 000ème et une carte au 1/1 000 000ème,* Vol. **2,** Société géologique de France.

Handy, M.R., Schmid, S.M., Bousquet, R., Kissling, E. & Bernoulli, D., 2010. Reconciling plate-tectonic reconstructions of Alpine Tethys with the geological–geophysical record of spreading and subduction in the Alps, *Earth-Sci. Rev.,* **102**(3–4), 121–158.

Helffrich, G., 2019. Comment on 'Crustal thickness across the Trans-European Suture Zone from ambient noise autocorrelations' by G. Becker and B. Knapmeyer-Endrun, *Geophys. J. Int.,* **217**(2), 906–908.

Kästle, E.D., El-Sharkawy, A., Boschi, L., Meier, T., Rosenberg, C., Bellahsen, N., Cristiano, L. & Weidle, C., 2018. Surface wave tomography of the Alps using ambient-noise and earthquake phase velocity measurements, *J. geophys. Res.,* **123**(2), 1770–1792.

Kennett, B., 2015. Lithosphere–asthenosphere P-wave reflectivity across australia, *Earth planet. Sci. Lett.,* **431,** 225–235.

Kennett, B., Saygin, E. & Salmon, M., 2015. Stacking autocorrelograms to map Moho depth with high spatial resolution in southeastern Australia, *Geophys. Res. Lett.,* **42**(18), 7490–7497.

Krischer, L., Megies, T., Barsch, R., Beyreuther, M., Lecocq, T., Caudron, C. & Wassermann, J., 2015. ObsPy: a bridge for seismology into the scientific python ecosystem, *Comput. Sci. Discov.,* **8**(1),.

Lai, X., Li, S. & Sun, Y., 2010. Exploration of fault-zone trapped waves at Pingtong town, in Wenchuan earthquake region, *Geod. Geodyn.,* **1**(1), 29–33.

Li, H., Zhu, L. & Yang, H., 2007. High-resolution structures of the Landers Fault Zone inferred from aftershock waveform data, *Geophys. J. Int.,* **171**(3), 1295–1307.

Lombardi, D., Braunmiller, J., Kissling, E. & Giardini, D., 2008. Moho depth and Poisson's ratio in the western-central Alps from receiver functions, *Geophys. J. Int.,* **173**(1), 249–264.

Lu, Y., Stehly, L., Paul, A. & Group, A.W., 2018. High-resolution surface wave tomography of the European crust and uppermost mantle from ambient seismic noise, *Geophys. J. Int.,* **214**(2), 1136–1150.

Lyu, C., Pedersen, H.A., Paul, A., Zhao, L. & Solarino, S., 2017. Shear wave velocities in the upper mantle of the western Alps: new constraints using array analysis of seismic surface waves, *Geophys. J. Int.,* **210**(1), 321–331.

Mroczek, S. & Tilmann, F., 2021. Joint ambient noise autocorrelation and receiver function analysis of the Moho, *Geophys. J. Int.,* **225**(3), 1920–1934.

Nakata, N., Gualtieri, L. & Fichtner, A., 2019. *Seismic Ambient Noise,* Cambridge Univ. Press.

Nicolas, A., Hirn, A., Nicolich, R. & Polino, R., 1990. Lithospheric wedging in the western Alps inferred from the ECORS-crop traverse, *Geology,* **18**(7), 587–590.

Nicole, B., Christian, S., Anne, P., Jean, V., Julien, F., François, T. & Marco, C., 2007. Local tomography and focal mechanisms in the south-western Alps: comparison of methods and tectonic implications, *Tectonophysics,* **432**(1–4), 1–19.

Nishida, K., 2017. Ambient seismic wave field, *Proc. Jpn. Acad., B,* **93**(7), 423–448.

Oren, C. & Nowack, R.L., 2016. Seismic body-wave interferometry using noise auto-correlations for crustal structure, *Geophys. J. Int.,* **208**(1), 321–332.

Phạm, T.-S. & Tkalčić, H., 2017. On the feasibility and use of teleseismic P wave coda autocorrelation for mapping shallow seismic discontinuities, *J. geophys. Res.,* **122**(5), 3776–3791.

Romero, P. & Schimmel, M., 2018. Mapping the basement of the Ebro Basin in Spain with seismic ambient noise autocorrelations, *J. geophys. Res.,* **123**(6), 5052–5067.

Roux, P., Sabra, K.G., Kuperman, W.A. & Roux, A., 2005. Ambient noise cross correlation in free space: theoretical approach, *J. acoust. Soc. Am.,* **117**(1), 79–84.

Ruigrok, E., Campman, X. & Wapenaar, K., 2011. Extraction of P-wave reflections from microseisms, *Comptes Rend. Geosci.,* **343**(8–9), 512–525.

Saygin, E., Cummins, P.R. & Lumley, D., 2017. Retrieval of the P wave reflectivity response from autocorrelation of seismic noise: Jakarta Basin, Indonesia, *Geophys. Res. Lett.,* **44**(2), 792–799.

Schimmel, M., 1999. Phase cross-correlations: design, comparisons, and applications, *Bull. seism. Soc. Am.,* **89**(5), 1366–1378.

Schimmel, M., Stutzmann, E. & Ventosa, S., 2018. Low-frequency ambient noise autocorrelations: waveforms and normal modes, *Seismol. Res. Lett.,* **89**(4), 1488–1496.

Schimmel, M. *et al.*, 2021. Seismic noise autocorrelations on mars, *Earth Space Sci.,* **8**(6), e2021EA001755,.

Taylor, G., Rost, S. & Houseman, G., 2016. Crustal imaging across the North Anatolian Fault Zone from the autocorrelation of ambient seismic noise, *Geophys. Res. Lett.,* **43**(6), 2502–2509.

Thouvenot, F., Paul, A., Frechet, J., Béthoux, N., Jenatton, L. & Guiguet, R., 2007. Are there really superposed Mohos in the southwestern Alps? New seismic data from fan-profiling reflections, *Geophys. J. Int.,* **170**(3), 1180–1194.

Tibuleac, I.M. & von Seggern, D., 2012. Crust-mantle boundary reflectors in Nevada from ambient seismic noise autocorrelations, *Geophys. J. Int.,* **189**(1), 493–500.

van Hinsbergen, D.J., Torsvik, T.H., Schmid, S.M., Maţenco, L.C., Maffione, M., Vissers, R.L., Gürer, D. & Spakman, W., 2020. Orogenic architecture of the Mediterranean region and kinematic reconstruction of its tectonic evolution since the Triassic, *Gondwana Res.,* **81,** 79–229.

Wapenaar, K., Draganov, D. & Robertsson, J.O., 2008. *Seismic Interferometry: History and Present Status,* Society of Exploration Geophysicists.

Yilmaz, O., 2001. *Seismic Data Analysis: Processing, Inversion, and Interpretation of Seismic Data,* Vol. **2,** Society of Exploration Geophysicists.

Zhao, L. *et al.*, 2015. First seismic evidence for continental subduction beneath the western Alps, *Geology,* **43**(9), 815–818.

Zhao, L., Paul, A. & Solarino, S., RESIF, 2016. Seismic network YP: CIFALPS temporary experiment (China-Italy-France Alps seismic transect) [data set], RESIF - Reseau Sismologique et geodesique Francais, doi:10.15778/RESIF.YP2012.

SUPPORTING INFORMATION

Supplementary data are available at *GJI* online.

Figure S1. We have used the 2-D *P*-wave velocity model by Zhao *et al.* (2015). The colour scale is given on the right-hand side.

Figure S2. (a) The variance of the daily autocorrelation stacks filtered in the 0.5–1 Hz frequency band is shown by the blue curve. The mean variance is indicated by the red dashed–dotted line. (b) The daily autocorrelation stacks of the complete data set. (c) The variance, blue curve, of only the summer daily stacks and (d) the winter daily stacks. The mean variance of the summer daily stacks (e) is ∼0.093 and higher than both the mean of the complete daily autocorrelation stacks (b) and the mean of only the winter daily stacks (f).

Figure S3. (a) Stations of the CIFALPS profile are plotted in elevation (m) from west to east. The position of Station CT30 is highlighted by the red upside down triangle. (b) The autocorrelation stacks of station CT30 are shown in the following frequency bands (Hz); (b) [0.3–0.8], (c) [0.3–0.9], (d) [0.3–1], (e) [0.4–1], (f) [0.5–1], (g) [0.5–2]. The autocorrelation stack in the 0.3–0.9 Hz frequency band, highlighted by the red rectangle, is selected for the final autocorrelation reflectivity profile along the CIFALPS transect (see Fig. 11). The prior Moho information by Zhao *et al.* (2015) is indicated by the pink dashed–dotted line, the arrival time of the manually picked Moho reflection is indicated by the green dashed–dotted line and the arrival times of the automatically picked Moho reflection by the blue dotted line. (h) Probability power spectrum.

The green rectangle highlights the high probability signal with little variance. (i) Spectrogram. Panels (h) and (i) are retrieved from: http://dx.doi.org/10.15778/RESIF.YP2012.

Figure S4. (a) Altitude profile in metres for the CIFALPS transect from west to east. Stations are shown by the inverted triangles; labels in red represent the station codes. The distance is measured from the Frontal Penninic Thrust (FPT) show in Fig. 1. (b) The green horizontal lines: Moho depths calculated from the manually picked arrival times of the Moho reflections. The green vertical dotted lines indicate the differences with the Moho depth determined by Zhao *et al.* (2015). The mean difference is 1.1 ± 1.3 km. (c) The blue horizontal lines: Moho depths calculated from the automatically picked arrival times of the Moho reflections. The blue vertical dotted lines indicate the differences with the Moho depth determined by Zhao *et al.* (2015). The mean difference is –1.8 ± 0.9 km. (d) The red vertical dotted lines indicate the differences between the (b) Moho depths from the manually picked arrival times, green lines and the (c) Moho depths from the automatically picked arrival times, blue lines. The mean difference is 2.8 ± 1.8 km.

Figure S5. Plots on the left: the final autocorrelation stacks of station CT01 in the 0.5–1 Hz frequency band with the automatically picked arrival times of the Moho reflections, blue dashed–dotted lines, based on the prior information by: (a) Zhao *et al.* (2015), pink dashed–dotted line, (b) Lu *et al.* (2018), brown dashed–dotted line and (c) the average of the aforementioned Moho information, cyan coloured line. (d) The prior intracrustal, red dashed–dotted line, and Moho information by Zhao *et al.* (2015). The envelope of the autocorrelation stack is the red line. Plots on the right-hand side: the second derivative of the envelope with the picked reflectivity changes or local maxima, blue circles, inside the *a priori* time window, grey window.

Figure S6. The probability density function of the power spectral densities (PSDs) of the stations CT14 and CT36 (figures retrieved from: http://dx.doi.org/10.15778/RESIF.YP2012). The black lines outline the periods along the *x*-axis at 1 s and ∼3.3 s, 1 Hz and 0.3 Hz, respectively. In addition, the noise level values of –120 and –150 db are outlined at the *y*-axis. The stations that are at different positions along the CIFALPS line show the same behaviour, the noise increases from –150 to –120 db for wavelengths from 1 s to ∼3.3 s.

Figure S7. The daily autocorrelation stacks for stations (a) CT01, (b) CT02, (c) CT03 and (d) CT04. The final stack of the daily stacks is shown in the graph on the right for each station. The prior Moho information by Zhao *et al.* (2015) is indicated by the pink dashed–dotted line and the arrival time of the Moho reflection from the automated method by Becker & Knapmeyer-Endrun (2018) by the blue dashed–dotted line. The arrival time of the Moho reflection from picking the most stable reflection along the daily stacks, green dashed–dotted line, is used for the final reflectivity profile. See Fig. S17(a) for better visualization of the stable reflection.

Figure S8. The daily autocorrelation stacks for stations (a) CT05, (b) CT06, (c) CT07 and (d) CT08. The final stack of the daily stacks is shown in the graph on the right for each station. The prior Moho information by Zhao *et al.* (2015) is indicated by the pink dashed–dotted line and the arrival time of the Moho reflection from the automated method by Becker & Knapmeyer-Endrun (2018) by the blue dashed–dotted line.

Figure S9. The daily autocorrelation stacks for stations (a) CT09, (b) CT10, (c) CT11 and (d) CT12. The final stack of the daily stacks is shown in the graph on the right for each station. The prior Moho information by Zhao *et al.* (2015) is indicated by the pink dashed–dotted line and the arrival time of the Moho reflection from the automated method by Becker & Knapmeyer-Endrun (2018) by the blue dashed–dotted line. The arrival time of the Moho reflection from picking the most stable reflection along the daily stacks, green dashed–dotted line, is used for the final reflectivity profile. See Figs S17(b) and (c) for better visualization of the stable reflections.

Figure S10. The daily autocorrelation stacks for stations (a) CT13, (b) CT14, (c) CT15 and (d) CT16. The final stack of the daily stacks is shown in the graph on the right for each station. The prior Moho information by Zhao *et al.* (2015) is indicated by the pink dashed–dotted line and the arrival time of the Moho reflection from the automated method by Becker & Knapmeyer-Endrun (2018) by the blue dashed–dotted line. The arrival time of the Moho reflection from picking the most stable reflection along the daily stacks, green dashed–dotted line, is used for the final reflectivity profile. See Fig. S17(d) for better visualization of the stable reflection.

Figure S11. The daily autocorrelation stacks for stations (a) CT17, (b) CT18, (c) CT19 and (d) CT20. The final stack of the daily stacks is shown in the graph on the right for each station. The prior Moho information by Zhao *et al.* (2015) is indicated by the pink dashed–dotted line and the arrival time of the Moho reflection from the automated method by Becker & Knapmeyer-Endrun (2018) by the blue dashed–dotted line. The arrival time of the Moho reflection from picking the most stable reflection along the daily stacks, green dashed–dotted line, is used for the final reflectivity profile. See Fig. S17(e) for better visualization of the stable reflection.

Figure S12. The daily autocorrelation stacks for stations (a) CT21, (b) CT22, (c) CT23 and (d) CT24. The final stack of the daily stacks is shown in the graph on the right for each station. The prior Moho information by Zhao *et al.* (2015) is indicated by the pink dashed–dotted line and the arrival time of the Moho reflection from the automated method by Becker & Knapmeyer-Endrun (2018) by the blue dashed–dotted line.

Figure S13. The daily autocorrelation stacks for stations (a) CT25, (b) CT26, (c) CT27 and (d) CT28. The final stack of the daily stacks is shown in the graph on the right for each station. The prior Moho information by Zhao *et al.* (2015) is indicated by the pink dashed–dotted line and the arrival time of the Moho reflection from the automated method by Becker & Knapmeyer-Endrun (2018) by the blue dashed–dotted line.

Figure S14. The daily autocorrelation stacks for stations (a) CT29, (b) CT30, (c) CT31 and (d) CT38. The final stack of the daily stacks is shown in the graph on the right for each station. The prior Moho information by Zhao *et al.* (2015) is indicated by the pink dashed–dotted line and the arrival time of the Moho reflection from the automated method by Becker & Knapmeyer-Endrun (2018) by the blue dashed–dotted line. The arrival time of the Moho reflection from picking the most stable reflection along the daily stacks, green dashed–dotted line, is used for the final reflectivity profile. See Figs S18(a)–(c) for better visualization of the stable reflections.

Figure S15. The daily autocorrelation stacks for stations (a) CT39, (b) CT40, (c) CT41 and (d) CT42. The final stack of the daily stacks is shown in the graph on the right for each station. The prior Moho information by Zhao *et al.* (2015) is indicated by the pink dashed–dotted line and the arrival time of the Moho reflection from the automated method by Becker & Knapmeyer-Endrun (2018) by the blue dashed–dotted line.

Figure S16. The daily autocorrelation stacks for stations (a) CT43, (b) CT44, (c) CT45 and (d) CT46. The final stack of the daily stacks is shown in the graph on the right for each station. The prior Moho information by Zhao *et al.* (2015) is indicated by the pink dashed–dotted line and the arrival time of the Moho reflection from the automated method by Becker & Knapmeyer-Endrun (2018) by the

blue dashed–dotted line. The arrival time of the Moho reflection from picking the most stable reflection along the daily stacks, green dashed–dotted line, is used for the final reflectivity profile. See Fig. S18(d) for better visualization of the stable reflection.

Figure S17. The stacks are plotted in shorter normalized time windows for better visualization of the stable reflections along the daily stacks for stations (a) CT04, (b) CT09, (c) CT11 (d) CT15 and (e) CT19.

Figure S18. The stacks are plotted in shorter normalized time windows for better visualization of the stable reflections along the daily stacks for stations (a) CT30, (b) CT31, (c) CT38 (d) CT46.